Check for updates

Polymer Composites

WILEY | spe INSPIRING PLASTICS PROFESSIONALS

RESEARCH ARTICLE OPEN ACCESS

Evaluation of Mechanical, Thermal, Rheological, and Biocompatibility Properties of Additively Manufactured Metal-Reinforced Biocomposites Optimized by Reinforcement Ratios and Printing Parameters

İbrahim Baki Sahin[1] | Bayram Sercan Bayram[2] | Begum Pinarbasi[3] | Pınar Yilgor[3] | Berzah Yavuzyegit[4,5] | İhsan Korkut[2]

[1]Department of Mechanical Engineering, Kırşehir Ahi Evran University, Kırşehir, Turkey | [2]Department of Manufacturing Engineering, Gazi University, Ankara, Turkey | [3]Department of Biomedical Engineering, Faculty of Engineering, Ankara University, Ankara, Turkey | [4]University of Portsmouth, School of Medicine, Pharmacy and Biomedical Sciences, Faculty of Science and Health, Portsmouth, UK | [5]Department of Mechanical Engineering, Recep Tayyip Erdoğan University, Rize, Turkey

Correspondence: Berzah Yavuzyegit (berzah.yavuzyegit@port.ac.uk)

Received: 9 September 2025 | **Revised:** 27 December 2025 | **Accepted:** 15 January 2026

Keywords: 3D printing | biomedical applications | composite filament | mechanical properties | multi-objective optimization | Taguchi design

ABSTRACT

Polylactic acid (PLA) is a biodegradable thermoplastic widely used in biomedical devices; however, its inherent brittleness and poor impact resistance restrict its use in mechanically demanding environments. This study investigates the mechanical, thermal, microstructural, and in vitro cytocompatibility performance of fused deposition modeling (FDM)-printed PLA/316L stainless steel (SS) biocomposites (3–15 wt%). Composite filaments were produced by melt compounding and printed using a Taguchi-based experimental design to assess the combined effects of reinforcement content and key FDM parameters, including raster orientation, nozzle temperature, and printing speed. Mechanical performance was evaluated through tensile, compressive, and Charpy impact testing, supported by microstructural and thermal characterization. A multi-response Taguchi–Gray Relational Analysis (GRA) was employed to identify optimal processing conditions. Under optimal conditions (15 wt% SS, 0° raster), tensile and compressive strengths reached 94 MPa and 102 MPa, respectively, alongside a significant improvement in impact energy absorption. Thermal analyses confirmed stability within the FDM processing window, while microstructural observations revealed a transition from homogeneous particle dispersion to agglomeration-driven defects at higher SS contents. Indirect cytotoxicity assessment following ISO 10993-5 guidelines using L929 fibroblasts demonstrated no acute cytotoxic response for any composite formulation after 72 h of extract exposure. Overall, the findings demonstrate that SS reinforcement, combined with controlled FDM parameters, yields PLA composites with substantially improved mechanical properties while maintaining short-term cytocompatibility, thereby supporting patient-specific, non-load-bearing biomedical applications.

1 | Introduction

Polylactic acid (PLA) is widely utilized biopolymer in the medical, packaging, and engineering sectors due to its biodegradability, cost-effectiveness, and mechanical properties [1–4]. In biomedical applications, bulk PLA's Young's modulus of 2–3 GPa, close to that of cancellous bone, together with its high biocompatibility, makes PLA a promising candidate for temporary orthopedic devices with reduced risk of stress shielding. Furthermore, its low melting temperature and glass transition range (~175°C and 55°C–65°C, respectively) enable efficient processing via fused deposition modeling (FDM),

This is an open access article under the terms of the Creative Commons Attribution License, which permits use, distribution and reproduction in any medium, provided the original work is properly cited.

© 2026 The Author(s). *Polymer Composites* published by Wiley Periodicals LLC on behalf of Society of Plastics Engineers.

Highlights

- PLA/316L SS biocomposites fabricated via melt compounding and FDM.
- Process parameters optimized using Taguchi–GRG design approach.
- Mechanical, thermal, and microstructural analyses integrated.
- Process–structure–property relations quantified in PLA/SS systems.
- SS particle dispersion evaluated across varying filler loadings.

facilitating the fabrication of complex, patient-specific implants [5–14].

Despite these advantages, PLA exhibits intrinsic brittleness, low impact strength, and limited thermal stability, which collectively restrict its use in load-bearing biomedical applications [5, 15–17]. Mechanical performance is further compromised by FDM-related defects such as weak interlayer bonding, void formation, and poor interfacial adhesion, resulting in significantly reduced tensile strength (as low as 5–17 MPa) and impact strength depending on processing parameters [18–23]. To address these limitations, extensive research has explored the incorporation of non-metallic fillers, including hydroxyapatite, bioactive glass, calcium phosphate ceramics, and carbon nanomaterials, to enhance mechanical, thermal, and biological properties [24–32]. However, hydrophilic ceramic fillers often exhibit poor interfacial compatibility with hydrophobic PLA, resulting in insufficient load transfer. Moreover, polymer blending strategies have yielded limited improvements; for example, PLA/PCL/HA systems frequently exhibit insufficient stiffness (1.35 GPa) and strength for hard tissue applications primarily due to the highly porous scaffold architecture and the polymer-dominated matrix designed to promote cell infiltration rather than load bearing [33–35], while graphene-based fillers show inconsistent strengthening effects [36–39].

Recently, the incorporation of biocompatible metal additives such as titanium (Ti), stainless steel (SS), and iron (Fe) has been shown to markedly enhance the strength and ductility of PLA-based composites [40–43]. For example, PLA/Ti composites with 5–10 vol% Ti have demonstrated ultimate tensile strengths of approximately 40 MPa and moduli reaching 4.0 GPa, the latter being approximately twice that of neat PLA [44]. Similarly, PLA reinforced with 316L SS exhibited increases in compressive strength (from 61 to 75 MPa), flexural strength (from 71 to 92 MPa), and fatigue strength (from 35 to 53 MPa) compared to unreinforced PLA [45].

However, the mechanical response of metal-reinforced PLA remains highly dependent on both filler dispersion and FDM processing conditions, including nozzle temperature, raster orientation, and printing speed [46–49]. Small variations in these process parameters can fundamentally alter the resulting microstructure, affecting particle agglomeration, interlayer void density, crystallinity, heat-affected zones, and interfacial bonding. These microstructural features directly dictate tensile load transfer, failure modes, anisotropy, and overall structural reliability [50–54].

Despite these advances, there is a notable lack of systematic, multi-response optimization studies that comprehensively evaluate the combined effects of reinforcement ratio and key FDM processing parameters on the mechanical, thermal, and biological properties of PLA/316L SS biocomposites. Furthermore, prior studies have explored the multivariate interactions among these parameters using advanced statistical tools, nor have they sufficiently addressed the relationship between microstructural integrity and mechanical performance in these systems. Therefore, there remains a critical need for holistic investigations that integrate process optimization, microstructural analysis, and in vitro biocompatibility assessment to inform the rational design of high-performance PLA/SS composites for biomedical applications.

In this study, we address these gaps by systematically investigating PLA/316L SS biocomposites produced via FDM, integrating Taguchi experimental design and Gray Relational Analysis (GRA) to optimize key mechanical responses, including tensile, compressive, and impact strengths, across a wide range of process parameters and reinforcement ratios. The comprehensive evaluation also encompasses thermal behavior, microstructural integrity, and in vitro cytocompatibility, providing a quantitative framework for the process-driven development of next-generation, load-bearing biomedical implants. The insights and optimized strategies provided here directly inform the design and fabrication of mechanically robust, biocompatible PLA/SS composites for use in patient-specific, load-bearing biomedical implants, addressing a critical need in regenerative medicine and orthopedic device engineering.

2 | Materials and Methods

The experimental methodology employed in this study is systematically presented in (Figure 1), detailing the sequential approach from raw material preparation to parameter optimization of 3D-printed PLA/SS composites. The research framework comprises seven distinct phases: (1) manufacturing of composite filaments, (2) structural, thermal, and morphological characterization, (3) statistical optimization using the Taguchi method, (4) mechanical testing and characterization, (5) optical microscopy, (6) validation, and (7) cytotoxicity testing for biocompatibility.

2.1 | Materials and Composite Filament Preparation for FDM

The PLA powder (Filameon, Turkey; sourced from NatureWorks, USA) had a molecular weight of ~100,000 g/mol, specific gravity of 1.24 g/cm^3, and a melt flow rate of 6 g/10 min (210°C/2.16 kg), as provided by the manufacturer. Spherical 316L stainless steel (SS) powder (Nanokar, Turkey) was used as reinforcement, with a chemical composition of Fe (70%), Cr (16%–18%), Ni (10%–14%), and Mo (2%–3%), a density of 7.9 g/cm^3, an average particle size (D50) of 44 μm (325 mesh), and a purity of 99.9%. The detailed PLA material properties are summarized in (Table 1).

15480569, 0, Downloaded from https://4spepublications.onlinelibrary.wiley.com/doi/10.1002/pc.70888 by Gazi University, Wiley Online Library on [04/02/2026]. See the Terms and Conditions (https://onlinelibrary.wiley.com/terms-and-conditions) on Wiley Online Library for rules of use; OA articles are governed by the applicable Creative Commons License

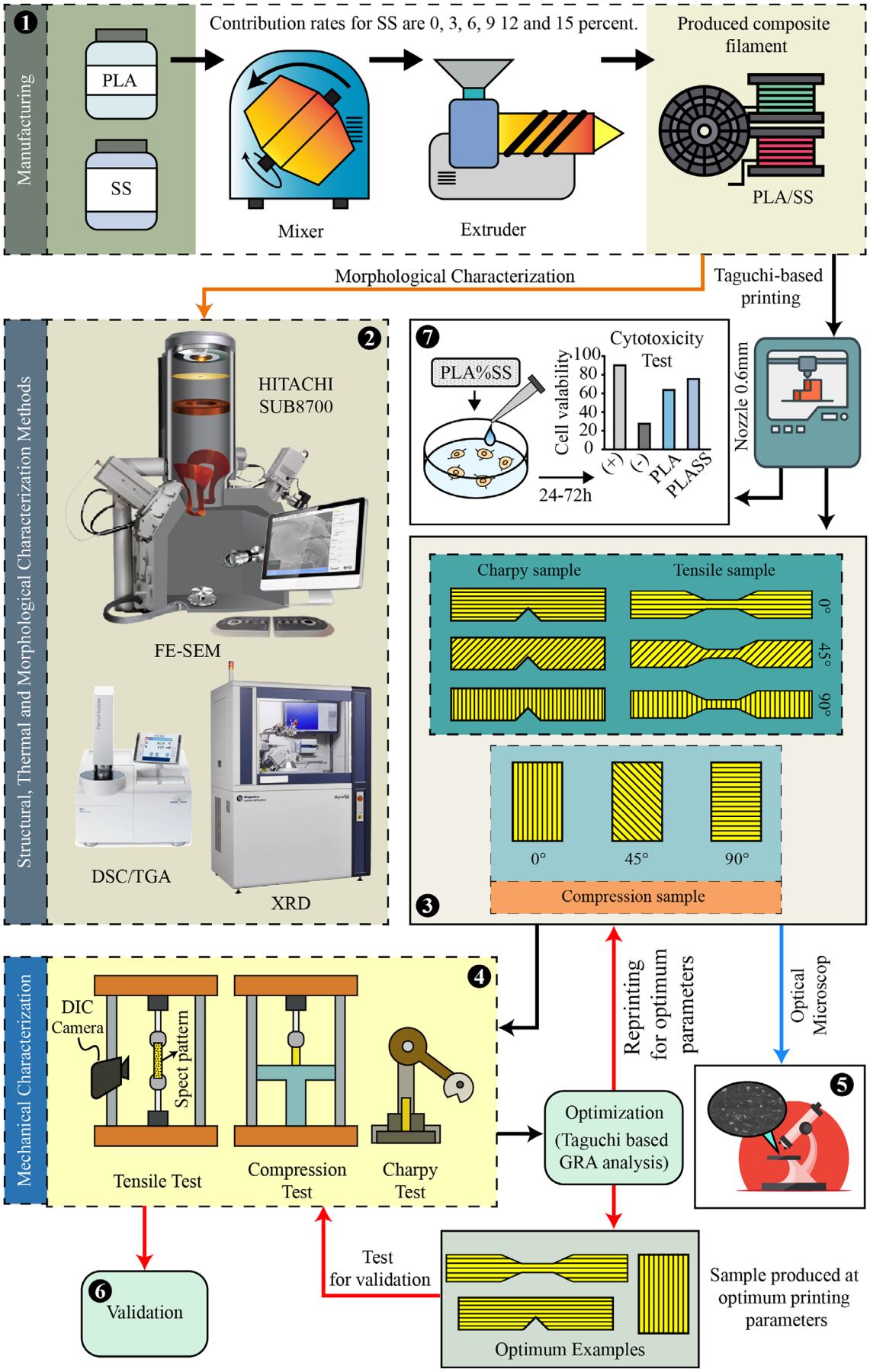


FIGURE 1 | Schematic workflow diagram of the experimental methodology used in this study.

15480569, 0, Downloaded from https://4spepublications.onlinelibrary.wiley.com/doi/10.1002/pc.70888 by Gazi University, Wiley Online Library on [04/02/2026]. See the Terms and Conditions (https://onlinelibrary.wiley.com/terms-and-conditions) on Wiley Online Library for rules of use; OA articles are governed by the applicable Creative Commons License

TABLE 1 | Characteristic properties of PLA material.

Property	Value
Density (g/cm^3)	1.24
Melting Temperature (°C)	175
Glass Transition Temperature (°C)	55–65
Yield Strength (MPa)	60
Elongation at Break (%)	6
Flexural Strength (MPa)	83
Heat Deflection Temperature (°C)	55

Composite blends were prepared at six different SS weight fractions: 0%, 3%, 6%, 9%, 12%, and 15%, selected based on preliminary trials and literature reports indicating that this range offers a suitable balance between mechanical reinforcement and processability [20]. Prior to processing, both PLA powders and SS powders were dried at 60°C for 12 h to eliminate moisture content. The dried materials were then mechanically mixed in a high-speed mixer for 15 min to achieve uniform dispersion of SS particles within the PLA matrix.

The homogenized mixtures were subsequently extruded into filaments using a single-screw filament extruder (3Devo Precision, 3Devo, Netherlands). Extrusion was performed at a constant temperature of 195°C ± 2°C, optimized according to the thermal behavior of the composite. A steady pulling speed of 10 mm/s was applied to maintain a consistent filament diameter of 1.75 mm suitable for FDM printing. The filament diameters were monitored at regular intervals using a digital caliper to ensure dimensional uniformity. After extrusion, the filaments were vacuum-sealed (DZ-400/2F, Wenzhou, China) at 20 mbar and stored in a moisture-controlled environment until further processing.

2.2 | Thermal and Structural Characterization of Filaments

The thermal properties of PLA/SS composite filaments (3–15 wt%) were characterized using Differential Scanning Calorimetry (DSC) and Thermogravimetric Analysis (TGA). DSC analyses were performed with a Hitachi DSC 7020 (Japan) to determine the glass transition temperature (T_g), melting temperature (T_m), and degree of crystallinity (X_c). Approximately 5–10 mg of sample was sealed in an aluminum pan and heated from 25°C to 300°C at a heating rate of 10°C/min under a nitrogen atmosphere. The degree of crystallinity was calculated using the following equation:

$$X_c(\%) = \frac{\Delta H_m - \Delta H_{cc}}{\Delta H_m^0} \times 100 \quad (1)$$

where ΔH_m is the melting enthalpy, ΔH_{cc} is the cold crystallization enthalpy, and ΔH_m^0 is the theoretical melting enthalpy of 100% crystalline PLA (93 J/g).

Thermal stability was further assessed using TGA on a Hitachi STA7300 (Japan). TGA measurements were performed under a nitrogen atmosphere at a heating rate of 10°C/min from 30°C to 200°C, specifically targeting the temperature range relevant to FDM processing. Limiting the analysis to this range enabled the evaluation of thermal stability and subtle degradation phenomena occurring within the actual processing window of FDM, where materials typically operate below 250°C.

The melt flow index (MFI) and melt volume rate (MVR) of the PLA/316L SS composite filaments were measured to assess their suitability for extrusion and printing. For each composition, MFI (g/10 min) and MVR (cm^3/10 min) tests were conducted according to ISO 1133-1, using a standard melt flow tester (Instron Ceast MF20, Italy). Tests were performed at 200°C, 235°C, and 270°C under a constant load (2.16 kg), and the average result of three replicate measurements was reported for each formulation. All tests were carried out in triplicate to ensure reproducibility.

2.3 | Experimental Design and Optimization

A Taguchi design of the experiment (DOE) approach was implemented to systematically investigate the effects of key FDM process parameters on the mechanical properties of PLA/316L SS composites [55]. The study considered four primary control factors: stainless steel weight fraction (A), printing orientation (B), nozzle temperature (C), and printing speed (D), each selected based on prior literature and preliminary investigations.

To efficiently explore the multivariable parameter space while minimizing the number of experimental runs, an L18 ($6^1 \times 3^3$) orthogonal array was adopted. This design generated 18 unique experimental conditions, each corresponding to a distinct combination of control factors (Table 2).

It is important to clarify that all graphical and tabulated results presented in this study, such as tensile, compressive, and impact performance, are based on unique parameter combinations defined by the Taguchi L18 orthogonal array. While figures may reference only SS content and raster orientation for readability (e.g., PLA6SS–0°), each data point inherently reflects a specific combination of four process parameters: reinforcement content, printing orientation, nozzle temperature, and printing speed, as detailed in (Table 2). Therefore, any interpretation of mechanical behavior should consider that observed trends result from the collective influence of these parameters rather than individual factors alone.

To quantitatively assess the effect of each factor on performance variation, signal-to-noise (S/N) ratios were calculated using the "larger-the-better" criterion, defined as:

$$\frac{S}{N} = -10.\log\left(\frac{1}{n}\sum_{i=1}^{n}\frac{1}{y_i^2}\right) \quad (2)$$

where y_i denotes the measured mechanical response and n is the number of repetitions for each condition.

Additionally, analysis of variance (ANOVA) was performed to statistically assess the significance and contribution ratio of

15480569, 0, Downloaded from https://4spepublications.onlinelibrary.wiley.com/doi/10.1002/pc.70888 by Gazi University, Wiley Online Library on [04/02/2026]. See the Terms and Conditions (https://onlinelibrary.wiley.com/terms-and-conditions) on Wiley Online Library for rules of use; OA articles are governed by the applicable Creative Commons License

TABLE 2 | Taguchi L18 orthogonal array used for experimental trials.

Run	SS wt.% (A)	Orientation (B)	Nozzle temp (C)	Printing speed (D)
1	0%	0°	200°C	205 mm/s
2	0%	45°	235°C	220 mm/s
3	0%	90°	270°C	235 mm/s
4	3%	0°	200°C	220 mm/s
5	3%	45°	235°C	235 mm/s
6	3%	90°	270°C	205 mm/s
7	6%	0°	235°C	205 mm/s
8	6%	45°	270°C	220 mm/s
9	6%	90°	200°C	235 mm/s
10	9%	0°	270°C	235 mm/s
11	9%	45°	200°C	205 mm/s
12	9%	90°	235°C	220 mm/s
13	12%	0°	235°C	235 mm/s
14	12%	45°	270°C	205 mm/s
15	12%	90°	200°C	220 mm/s
16	15%	0°	270°C	220 mm/s
17	15%	45°	200°C	235 mm/s
18	15%	90°	235°C	205 mm/s

each processing parameter to the total variation in mechanical responses. All statistical evaluations were conducted at a 95% confidence level ($p < 0.05$).

The experimental samples produced according to these parameter combinations were subsequently subjected to mechanical characterization, including tensile, compressive, and impact testing, as described in the following section.

2.4 | Mechanical Testing of Printed Specimens

Mechanical testing was conducted to assess the tensile, compressive, and impact properties of FDM-printed PLA/SS composites. All specimens were produced under processing conditions defined by the Taguchi design (orientation and nozzle temperature combinations). Prior to testing, all samples were conditioned at 23°C ± 2°C and 50% ± 5% relative humidity for 24 h to ensure moisture equilibrium.

All mechanical tests were conducted using a universal testing system (Instron 5969, USA). The machine was equipped with a 5 kN load cell for tensile testing and a 50 kN load cell for compressive testing. Load cells were calibrated in accordance with ISO 7500-1 standards. For each configuration, tests were performed in a minimum of 2 replicates to ensure repeatability, and the resulting data were analyzed using mean values, standard deviations, and one-way ANOVA at a 95% confidence level.

2.5 | Tensile Testing

Tensile properties were evaluated according to ASTM D638, using Type V dog-bone specimens with dimensions of 63.5 mm overall length, 9.53 mm overall width, and 3.2 mm thickness. Specimens were printed at orientations of 0°, 45°, and 90°, where 0° denotes raster alignment with the loading direction. The crosshead speed was set to 5 mm/min during testing using the 5 kN load cell.

A non-contact optical method was employed to monitor deformation (Figure 2). Specimens were prepared with a matte black base and a random white speckle pattern to maximize surface contrast. Image acquisition was performed using a high-resolution digital camera (Nikon D7500, 20.9 MP, 4.2 μm, 8 fps) positioned orthogonally to the gauge section at 3-s intervals. This approach was preferred over conventional extensometers to avoid potential surface damage and stress concentrations from mechanical contact [56]. Moreover, optical techniques enable full-field strain measurement, facilitating the detection of local strain heterogeneities that point-based devices cannot capture [57]. Non-contact methods also increase operator safety during specimen failure and provide greater flexibility regarding specimen geometry and alignment without recalibration [58].

Image sequences (10–30 frames per test) were analyzed using ImageJ software. Red markers were manually tracked along the gauge region, and strain was calculated using a pixel-to-length calibration based on an initial gauge length of 10 mm:

$$\varepsilon = \frac{l_i - l_0}{l_0} \tag{3}$$

where l_0 is the initial gauge length and l_i is the instantaneous distance between tracked points in each frame.

2.6 | Compressive Testing

Compressive strength was measured according to ASTM D695, using cylindrical specimens with a diameter of 12.7 mm and a height of 25.4 mm, maintaining the 2:1 height-to-diameter aspect ratio required by the standard. Tests were performed using a 50 kN load cell at a constant crosshead speed of 5 mm/min.

Stress–strain data were acquired throughout the tests, from which the compressive modulus and the maximum compressive strength were determined. The compressive modulus was calculated from the linear elastic portion of the stress–strain curve. In this study, the strain was derived directly from the crosshead displacement of the testing machine, following established ASTM D695 procedures for rigid polymeric materials where direct extensometry is often not feasible due to specimen geometry and potential instability during loading.

15480569, 0, Downloaded from https://4spepublications.onlinelibrary.wiley.com/doi/10.1002/pc.70888 by Gazi University, Wiley Online Library on [04/02/2026]. See the Terms and Conditions (https://onlinelibrary.wiley.com/terms-and-conditions) on Wiley Online Library for rules of use; OA articles are governed by the applicable Creative Commons License

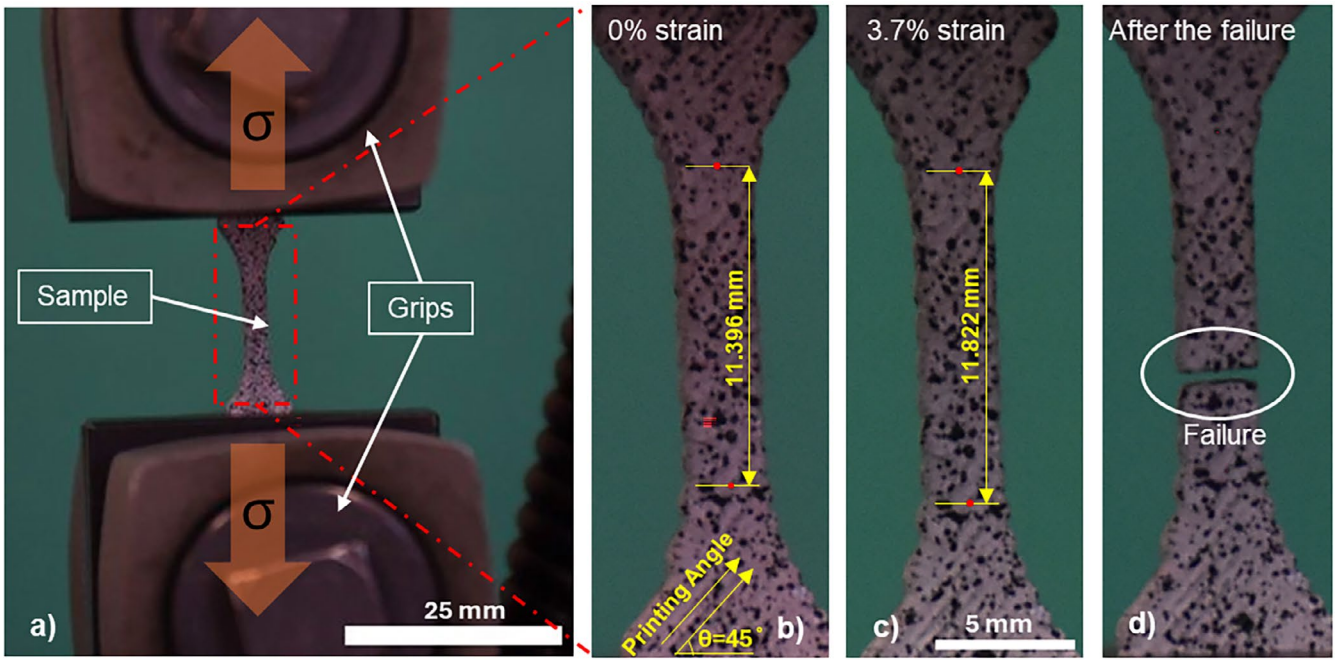


FIGURE 2 | Tensile testing setup and deformation sequence of a 3D-printed PLA/SS specimen of PLA12SS-45°. (a) Overall test configuration showing the mounted specimen held between grips, subjected to uniaxial tensile stress (σ). (b) Initial undeformed state (0% strain), (c) strained state at 3.7% elongation, and (d) final failure of the specimen, occurring in the gauge section. The sample was fabricated with a 45° raster angle relative to the loading direction, as indicated in (b). A non-contact optical strain measurement technique was employed by applying a black base coat followed by a white speckle pattern on the specimen surface.

TABLE 3 | Mechanical Testing Summary.

Test type	Standard	Specimen type	Dimensions (mm)	Speed	Load cell	Orientation (s)
Tensile Test	ASTM D638	Type V dog-bone	63.5 × 9.53 × 3.2	5 mm/min	5 kN	0°, 45°, 90°
Compressive Test	ASTM D695	Cylinder	Ø12.7 × 25.4 (h/d = 2:1)	5 mm/min	50 kN	0°, 45°, 90°
Impact (Charpy)	ASTM D6110	Notched rectangular bar	80 × 10 × 4, notch: 2 mm/45°		N/A	0°, 45°, 90°

2.7 | Impact Testing

Impact resistance of the composite specimens was evaluated using Charpy impact testing in accordance with ASTM D6110. Rectangular notched specimens with dimensions of 80 mm (length) × 10 mm (width) × 4 mm (thickness) were prepared. Each specimen contained a 2 mm deep V-notch machined at a 45° angle with a standard notch root radius of 0.25 mm, as specified in ASTM D6110.

All tests were conducted at ambient laboratory conditions (23°C ± 2°C, 50% ± 5% RH) using a pendulum-type impact tester (Ceast 9050, Instron, USA) equipped with an appropriately calibrated hammer to ensure the absorbed energy remained within 10%–90% of the instrument's capacity. The absorbed energy (expressed in joules) was recorded for each specimen and used as a direct measure of impact toughness.

For each testing condition, at least two specimens were tested to ensure repeatability, and the resulting values were analyzed as mean ± standard deviation. A summary of the mechanical testing procedures, specimen geometries, and test parameters is provided in (Table 3).

2.8 | Microstructural Characterization

The microstructural characterization of PLA/SS composite filaments and printed specimens was conducted to evaluate SS particle distribution, interfacial quality, and failure mechanisms. Initially, specimens were embedded in epoxy resin and, after complete curing, subjected to sequential grinding with silicon carbide abrasive papers of 800, 1200, and 2500 grit sizes. Polishing was subsequently performed using a 1 μm diamond suspension with an oil-based lubricant. The choice of an oil-based medium, rather than a water-based lubricant, was made to prevent hydrolytic degradation or swelling of the PLA matrix, which can lead to artifacts or inaccuracies in microstructural and elemental analyses due to water–polymer interactions. After each grinding and polishing stage, samples were ultrasonically cleaned in ethanol for 5 min to remove surface debris and residues, followed by drying under ambient airflow.

15480569, 0, Downloaded from https://4spepublications.onlinelibrary.wiley.com/doi/10.1002/pc.70888 by Gazi University, Wiley Online Library on [04/02/2026]. See the Terms and Conditions (https://onlinelibrary.wiley.com/terms-and-conditions) on Wiley Online Library for rules of use; OA articles are governed by the applicable Creative Commons License

Microstructural and compositional analysis was conducted using a field-emission scanning electron microscope (SEM, ZEISS Sigma 300VP, Germany) operating at accelerating voltages of 10–15 kV, with a working distance of approximately 10 mm. SEM imaging was performed at magnifications ranging from 50× to 5000×, depending on the specific feature analyzed. Non-conductive samples were sputter-coated with a 5 nm gold/palladium alloy layer to prevent surface charging during high-vacuum operation.

Elemental mapping and quantitative analysis were carried out using an Oxford Instruments energy-dispersive X-ray spectroscopy (EDX) system, employing a 90-s acquisition time per frame for elemental maps. Quantification was performed using a standardless ZAF correction model. For each specimen, multiple regions were examined to ensure statistical consistency across particle distribution and interfacial observations.

Optical microscopy (Olympus SZ61TR, Japan) was utilized to perform preliminary microstructural screening. Observations were conducted on ground cross-sections (longitudinal and transverse). Special attention was given to SS particle dispersion homogeneity, structural anisotropy, shear band formation, interlayer delamination, and local failure features.

Additionally, XRD analysis of the composite with the highest SS content was carried out in the 20°–80° 2θ range using a Bruker D8 Advance device (Cu Kα, $\lambda = 1.54056$ Å) at a scanning speed of 0.04°/second. Diffraction patterns were processed using HighScore Plus (PANalytical), and phase identification was carried out via the ICDD PDF-4+ database to determine crystalline phases, lattice parameters, and potential phase transformations.

2.9 | Filler Content Quantification

To quantify the actual SS content within the PLA matrix, optical microscopy was employed in combination with image analysis. Two representative micrographs were obtained for each composite formulation using an optical microscope at consistent magnification. The acquired RGB images were imported into ImageJ software for processing.

Each image was first converted to 8-bit grayscale to facilitate pixel-based thresholding. A median filter was applied to reduce image noise and enhance the contrast between the polymer matrix and stainless steel particles. Following image enhancement, thresholding was used to segment the SS particles from the surrounding PLA phase. The area fraction of the SS was then calculated by analyzing the proportion of thresholded regions relative to the total image area. This procedure was repeated for all specimens, and the resulting values were averaged to estimate the effective filler content.

2.10 | In Vitro Cytotoxicity Assessment

Cytocompatibility of PLA and PLA/316L SS composite samples was evaluated using an indirect cytotoxicity test according to ISO 10993-5, utilizing a Minimum Essential Medium (MEM) extraction method. The experimental groups included neat PLA and PLA composites reinforced with 3, 6, 9, 12, and 15 wt% stainless steel particles. Additionally, positive and negative control groups were used for comparative assessment.

Composite samples were first sterilized by immersion in 70% ethanol and subsequently exposed to ultraviolet (UV) radiation for 30 min per side. After sterilization, the samples were thoroughly rinsed with phosphate-buffered saline (PBS). For extraction, sterilized PLA and PLA/SS composite samples were immersed in a cell culture medium (Dulbecco's Modified Eagle's Medium, DMEM) supplemented with 10% fetal bovine serum (FBS) and 1% penicillin-streptomycin. Samples were incubated for 24 h at 37°C under continuous shaking conditions (60 rpm). Following incubation, extraction media were collected, filtered through a sterile 0.45 μm membrane, and stored in sterile falcon tubes until testing.

L929 mouse fibroblast cells were cultured in high-glucose DMEM supplemented with 10% FBS and 1% penicillin–streptomycin, seeded into T75 culture flasks, and incubated for 24 h at standard culture conditions (37°C, 5% CO2, high humidity). Subsequently, the cells were detached by trypsinization, counted, and seeded into 24-well plates at a density of 10,000 cells/cm^2 (approximately 20,000 cells per well). Cells were incubated for an additional 24 h until approximately 70% confluency was reached, confirmed by microscopic evaluation. Afterward, 500 μL of the extract medium from each experimental group was added to each well.

The cell morphology, confluency, and viability were assessed at intervals of 24, 48, and 72 h following the exposure to the extraction media. Morphological changes, the presence of detached or dead cells, and overall cell layer confluency were evaluated by phase-contrast microscopy at 10× and 40× magnification. At the end of 72 h, cell viability was quantitatively analyzed using Alamar Blue staining, which detects the metabolic activity of viable cells through a colorimetric change mediated by cellular dehydrogenase enzymes.

Microscopic observations and quantitative analyses were compared against negative control results and graded according to defined criteria for cell layer confluency, detached cell counts, morphological alterations, and growth inhibition. Scores from these criteria were averaged and combined to yield a final cytotoxic response index ranging from 0 (no cytotoxicity) to 8 (severe cytotoxicity). This index facilitated the determination of the materials' cytotoxic potential according to ISO 10993-5 standards.

3 | Results

In this section, the effects of 316L SS reinforcement and fused deposition modeling (FDM) process parameters on the thermal, rheological, microstructural, mechanical, and biological performance of PLA-based composites are systematically presented. The outcomes are organized according to experimental stages, including thermal transitions, flow behavior, filler dispersion, mechanical responses under tensile, compressive, and impact loading, as well as in vitro cytocompatibility. In addition, statistical optimization using Taguchi–GRA is reported to identify the most influential factors and optimal processing conditions.

15480569, 0, Downloaded from https://4spepublications.onlinelibrary.wiley.com/doi/10.1002/pc.70888 by Gazi University, Wiley Online Library on [04/02/2026]. See the Terms and Conditions (https://onlinelibrary.wiley.com/terms-and-conditions) on Wiley Online Library for rules of use; OA articles are governed by the applicable Creative Commons License

3.1 | Thermal Properties and Crystallization Behavior

Differential scanning calorimetry and thermogravimetric analysis revealed a clear, filler-dependent modification in the thermal response of PLA/316L SS composites. As shown in (Figure 3) and (Figure S1), the glass transition temperature (T_g) increases progressively with SS loading, rising from ~60°C at 3 wt% SS to ~73°C at 15 wt%. The upward shift and the slightly more defined transition region indicate restricted amorphous chain mobility, consistent with stronger polymer–particle interactions and reduced segmental freedom at higher filler contents.

Melting behavior also exhibits composition-dependent changes. Based on the DSC peak temperatures, the melting peak (T_m) is located in a narrow range (~149°C at 3 wt% and ~144°C at 15 wt%), showing a slight downward shift with increasing SS content (Table 4). In parallel, the melting endotherm becomes broader at higher filler levels, which suggests increased heterogeneity in crystalline populations and reduced lamellar perfection. This broadening is consistent with the role of SS particles as physical constraints that perturb lamellar organization during crystallization and melting.

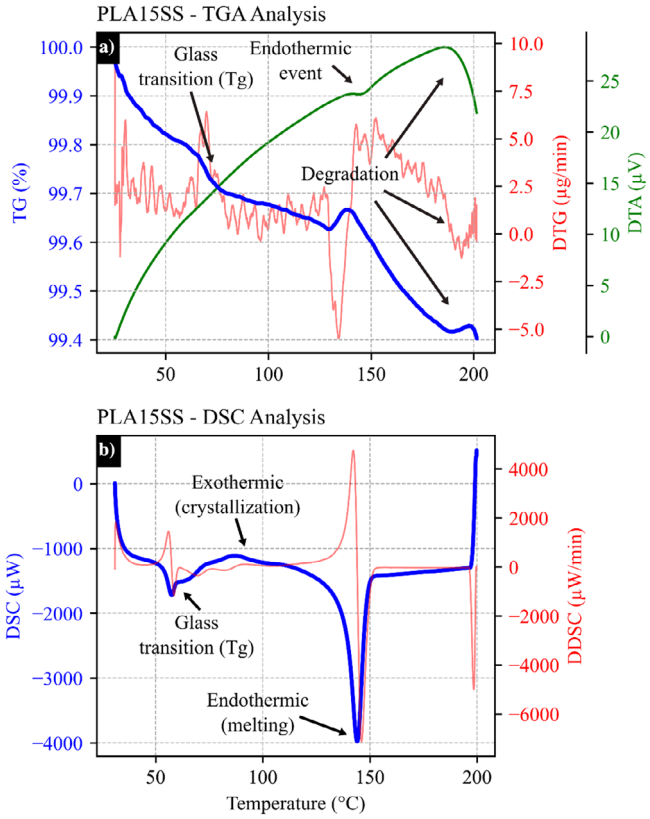


FIGURE 3 | TGA (a) and DSC (b) thermograms of 15 wt% PLA/SS composites.

Cold crystallization behavior demonstrates strong sensitivity to SS content (Figure S1), showing pronounced exothermic cold-crystallization features in the 3–9 wt% composites, whereas the signal diminishes markedly at 12 wt% and becomes negligible at 15 wt%. This trend aligns with the progressive reduction in ΔH_{cc} (from 26.1 J/g at 3 wt% to 3.1 J/g at 15 wt%; Table 4), indicating that increasing filler loading suppresses cold crystallization during heating by limiting chain rearrangement and reducing the fraction of mobile amorphous segments.

The degree of crystallinity (Xc), calculated from the enthalpy balance between melting and cold crystallization, remains relatively low across the series (≈3%–5%; Table 4). This outcome reflects the close magnitude of ΔHm and ΔHcc values, indicating that a substantial portion of the crystalline fraction observed during heating is formed through cold crystallization rather than being present as stable crystals before heating. At higher SS loadings, the strong decrease in ΔHm together with the disappearance of the cold-crystallization signal suggests that both crystal growth and reorganization become increasingly hindered, likely due to geometric confinement and reduced chain mobility in the vicinity of SS particles.

TGA results in (Figure 3) and (Figure S1) show minimal mass loss below 200°C for all compositions. The TG/DTG profiles confirm that neither neat PLA nor the PLA/SS composites undergo substantial thermal degradation within the FDM-relevant processing window. The increase in residual mass with increasing SS content is attributed to the inert metallic fraction and supports the thermal stability of the composites during printing.

3.2 | Rheological Characterization of Filaments

To assess the processability of PLA/316L SS composite filaments for FDM applications, rheological properties including melt flow index (MFI) and melt volume rate (MVR) were characterized for each formulation at three different temperatures (200°C, 235°C,

TABLE 4 | Thermal properties of PLA/SS composites with varying SS contents as determined by DSC and TGA analyses. Tg: Glass transition temperature; Tm: Melting temperature; ΔHcc: Cold crystallization enthalpy; ΔHm: Melting enthalpy; Xc: Degree of crystallinity; Values represent mean ± standard deviation ($n = 3$).

SS (wt %)	Tg (°C)	Tm (°C)	ΔHcc (J/g)	ΔHm (J/g)	Xc (%)
3	60.2 ± 0.5	149 ± 2	26.1 ± 1.5	29.2 ± 1.8	3.44 ± 2.60
6	63.1 ± 0.7	147 ± 2	28.3 ± 1.8	31.1 ± 2.1	3.20 ± 3.16
9	66.4 ± 0.9	146 ± 2	24.7 ± 2.1	27.8 ± 2.5	3.66 ± 3.86
12	69.2 ± 1.1	145 ± 2	15.2 ± 2.8	18.9 ± 3.1	4.52 ± 5.10
15	72.8 ± 1.3	144 ± 2	3.1 ± 1.2	6.7 ± 2.8	4.55 ± 3.85

15480569, 0, Downloaded from https://4spepublications.onlinelibrary.wiley.com/doi/10.1002/pc.70888 by Gazi University, Wiley Online Library on [04/02/2026]. See the Terms and Conditions (https://onlinelibrary.wiley.com/terms-and-conditions) on Wiley Online Library for rules of use; OA articles are governed by the applicable Creative Commons License

and 270°C). As shown in Figure S2, both MFI and MVR values increased with rising temperature across all SS contents apart from 6% SS content. The most dramatic temperature effect was observed in the 6% SS composite, where MFI increased from 1.9 g/10 min at 200°C to 3.9 g/10 min at 235°C and then decreased to nearly 3 g/10 min. For the 3% SS composite, the MFI increased from 1.8 g/10 min at 200°C to 2.4 g/10 min at 270°C.

At fixed temperatures, the effect of SS content followed different patterns. At 200°C, MFI values rose progressively from 1.8 g/10 min at 3% SS to 3.4 g/10 min at 15% SS. At 235°C, the highest MFI (3.9 g/10 min) was observed at 6% SS content, while at 270°C, MFI values generally increased with SS content.

For MVR measurements, similar temperature-dependent behavior was observed. The 6% SS composite showed the highest MVR value (2.91 cm^3/10 min) at 270°C. At 9% SS content, a notable difference was observed between MVR values at different temperatures, with 1.19 cm^3/10 min at 200°C increasing to 2.44 cm^3/10 min at 270°C.

3.3 | Microstructural Analysis of the Filament Cross-Sections

The optical micrographs of the PLA/SS biocomposites in the normal (ND), longitudinal (LD), and transverse (TD) directions are presented in (Figure 4), revealing distinct morphological trends correlated with SS content. At PLA3SS, the microstructure showed a fine and uniform dispersion of particles in the ND, with no visible clustering. The LD section exhibited subtle interlayer micro-defects aligned along the build direction, while the TD section revealed faint flow lines. For PLA6SS, slight particle clustering emerged in the ND, whereas the LD section showed heavy agglomeration of SS particles surrounded by polymer-rich halos. TD sections continued to exhibit flow lines, although more pronounced than in PLA3SS.

The PLA9SS samples demonstrated the onset of periodically aligned interlayer voids in the ND direction. LD sections revealed recurring interlayer micro-defects, and moderate agglomeration was observed across the TD section. At PLA12SS, the ND section showed highly ordered, periodically aligned interlayer voids with an otherwise homogeneous dispersion of the SS phase. LD sections displayed well-defined micro-defects running parallel to the build direction, while the TD microstructure appeared morphologically stable. In PLA15SS, the microstructural characteristics further intensified, with densely packed interlayer voids periodically aligned across the ND. The LD revealed well-developed micro-defects, while the TD section maintained an apparently homogeneous but particle-dense texture (Figure 5), presents supporting SEM, quantitative, and XRD data. Microscopic examination of the PLA filament, as well as PLA filaments reinforced with stainless steel, revealed the presence of directionally aligned features along the extrusion axis (Figure 5a). Such orientation patterns are not exclusive to neat PLA but were also observed in all blend formulations.

Dispersed reinforcement particles, observed as bright white regions in the SEM images (Figure 5b), confirmed by the EDX analysis performed on several points (Figure S3). These particles appear relatively well-distributed in most regions. However, localized regions of particle agglomeration were also evident (Figure 5b), shown in the lower left quadrant of the examined area.

In addition, several matrix deficiency zones were identified, appearing as dark voids or unfilled regions surrounding or adjacent to reinforcement particles. As shown in (Figure 5c), several spherical voids with smooth, circular perimeters were identified. In addition to spherical voids, several irregularly shaped cavities were also observed (Figure 5c). Quantitative image analysis was performed to validate the actual filler content in the PLA/SS composites (Figure 5d). The measured stainless steel area fractions obtained from threshold-based processing of optical micrographs using ImageJ closely matched the nominal filler loadings.

The X-ray diffraction (XRD) analysis presented in Figure 5e confirms the crystallographic structure of the 316 L stainless steel particles utilized in the composite formulations. The notable peaks observed at approximately 43.5°, 50.7°, and 74.6° correspond to the (111), (200), and (220) crystallographic planes of the austenitic phase, with good crystalline quality and phase purity. The sharpness and intensity of these peaks maintain a highly ordered crystal structure.

3.4 | Mechanical Properties of PLA/SS Composites

3.4.1 | Tensile Test

Tensile stress–strain behavior of the PLA/SS composites under different raster orientations is illustrated in (Figure 6), while the corresponding mechanical property metrics (elastic modulus, yield strength, ultimate tensile strength (UTS), and strain-to-failure) are summarized in Figure S4. For clarity and readability, the figure labels indicate only the SS content and build orientation (e.g., PLA6SS–0°); however, each data point corresponds to a unique combination of four processing parameters as defined by the Taguchi L18 orthogonal array: SS content, printing orientation, nozzle temperature, and printing speed. As such, the mechanical behavior observed should be interpreted as the outcome of these combined parameters, not solely as a function of SS content or orientation.

The highest elastic modulus was obtained for PLA15SS at 0°, reaching approximately 350 MPa, which represents a 20% increase compared to neat PLA at the same orientation. All samples printed at 0°, except for PLA3SS and PLA9SS, exhibited elastic modulus values above 330 MPa. For specimens printed at 90°, all composites showed elastic modulus values exceeding 250 MPa. In 45° printed specimens, elastic modulus values for PLA3SS and PLA6SS were lower than that of neat PLA (250 MPa), while PLA9SS, PLA12SS, and PLA15SS exhibited progressively higher modulus values, with PLA15SS reaching approximately 270 MPa. The strain-to-failure increased with SS content in specimens printed at 0°, rising from 1.5% for neat PLA to 3.5% for PLA15SS, with a plateau observed beyond 9% SS content. For specimens printed at 45° and 90°, strain-to-failure values for all SS-reinforced composites exceeded those of neat PLA, reaching maximum values of 3.4% at 45° and 3.2% at 90°.

15480569, 0, Downloaded from https://4spepublications.onlinelibrary.wiley.com/doi/10.1002/pc.70888 by Gazi University, Wiley Online Library on [04/02/2026]. See the Terms and Conditions (https://onlinelibrary.wiley.com/terms-and-conditions) on Wiley Online Library for rules of use; OA articles are governed by the applicable Creative Commons License

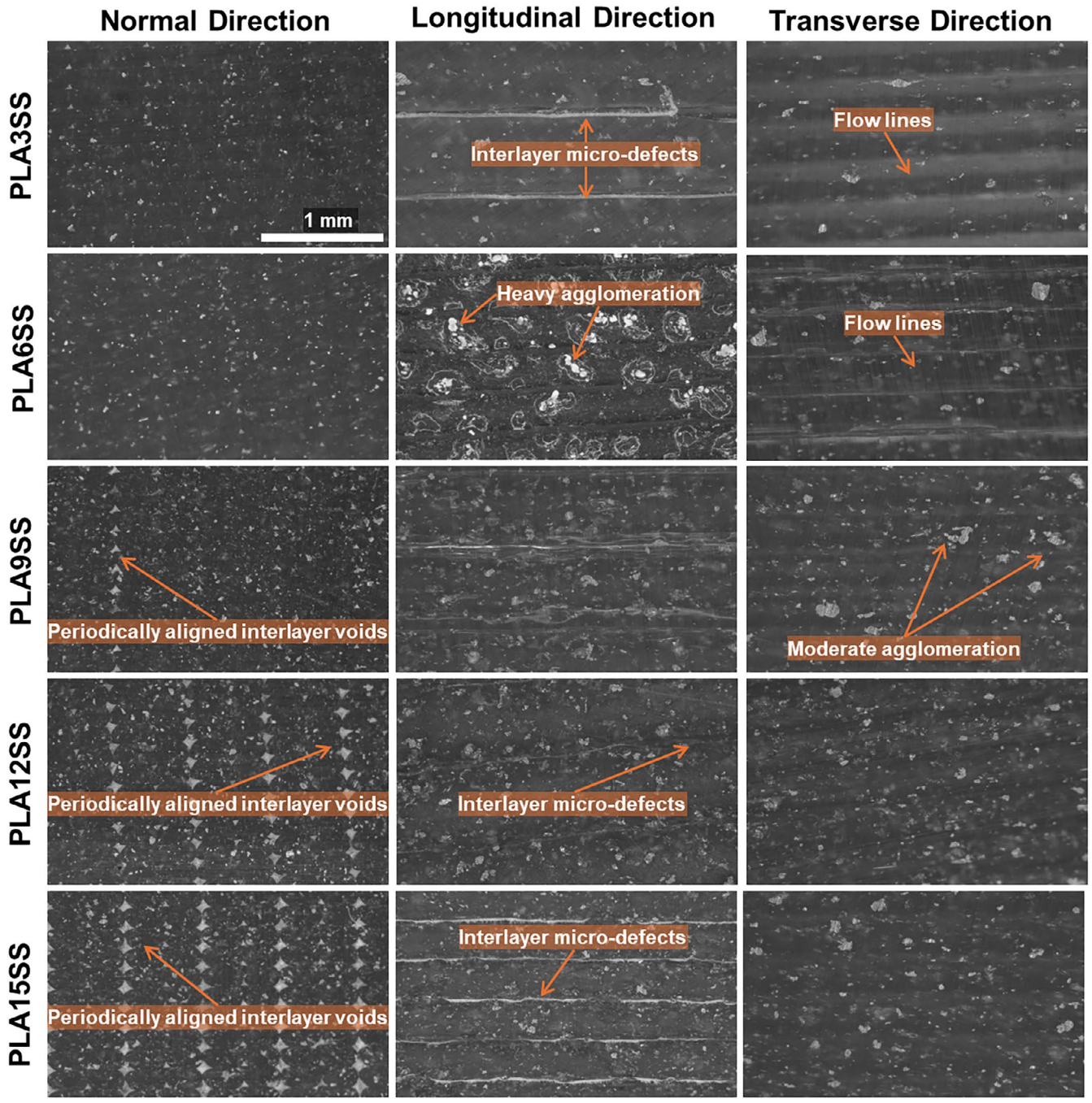


FIGURE 4 | Representative optical micrographs of PLA/SS biocomposites in three orthogonal directions: Normal (ND), longitudinal (LD), and transverse (TD) for varying SS content (3–15 wt%). Microstructural features such as interlayer micro-defects, agglomeration, flow lines, and periodically aligned interlayer voids are indicated. The evolution of these features with increasing SS content is observed across the different compositions.

The highest yield strength (72 MPa) was recorded for PLA12SS printed at 45°, nearly triple that of neat PLA at the same orientation. This composition also maintained high yield strength (~70 MPa) across all build angles. Lower yield values (~10 MPa) were observed in PLA3SS and PLA6SS. The ultimate tensile strength peaked at ~100 MPa for PLA15SS printed at both 0° and 90°, while PLA6SS and PLA12SS across all orientations yielded intermediate values (80–88 MPa). In contrast, neat PLA displayed substantially lower UTS, ranging from 28 MPa (45°) to 49 MPa (90°).

3.4.2 | Compression Test

The compressive stress–strain curves in (Figure 7) reveal different behavior compared to tensile properties. The quantitative mechanical properties derived from these curves are summarized in Figure S5, covering compressive modulus, yield strength, ultimate strength, and strain-to-failure.

Compressive modulus values ranged from approximately 600 MPa to 2100 MPa, with 3–6 wt% SS content delivering the

15480569, 0, Downloaded from https://4spepublications.onlinelibrary.wiley.com/doi/10.1002/pc.70888 by Gazi University, Wiley Online Library on [04/02/2026]. See the Terms and Conditions (https://onlinelibrary.wiley.com/terms-and-conditions) on Wiley Online Library for rules of use; OA articles are governed by the applicable Creative Commons License

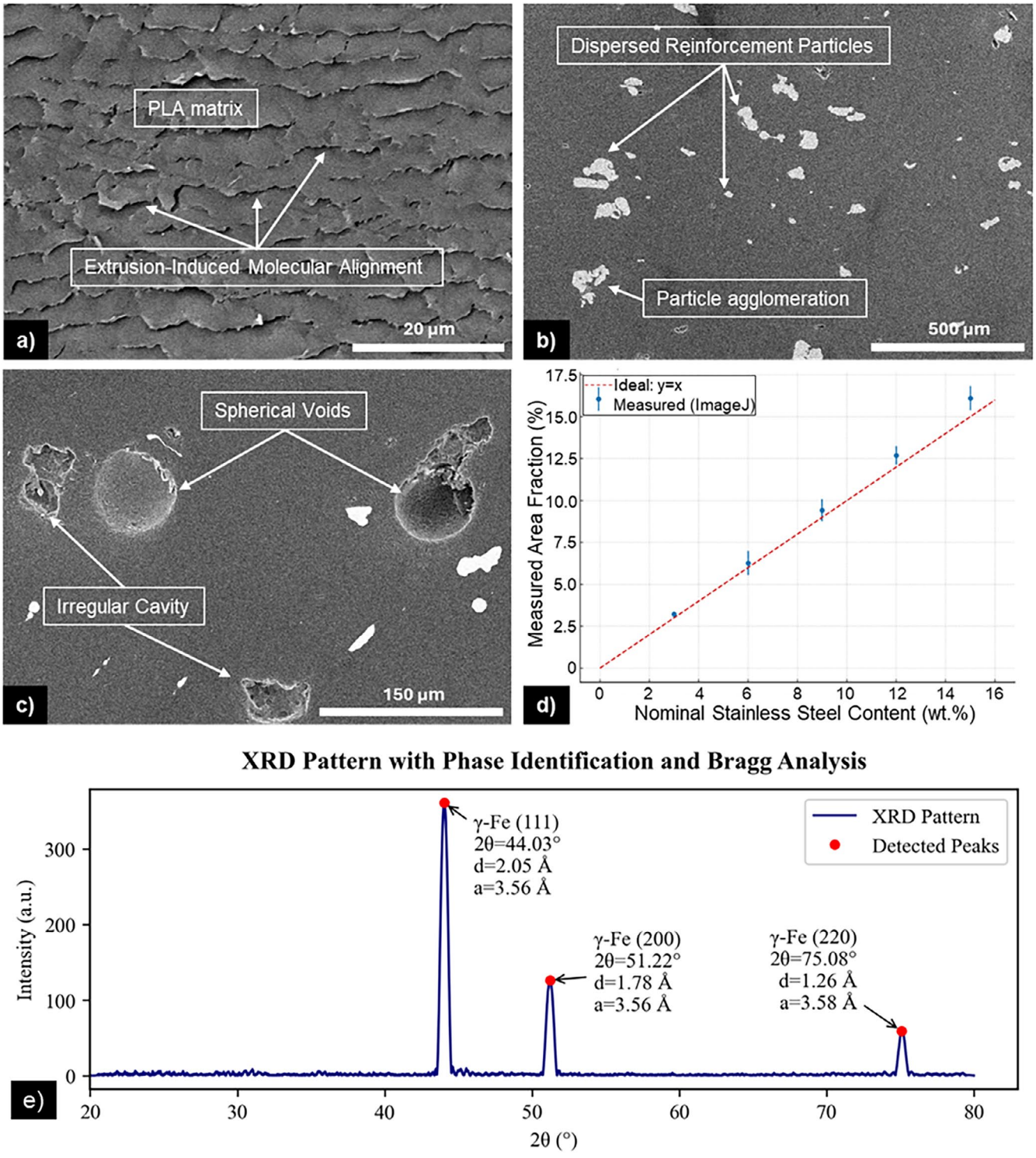


FIGURE 5 | Representative SEM micrographs and image analysis of PLA-based filaments. (a) Neat PLA showing extrusion-induced molecular alignment. (b) Dispersed and agglomerated stainless steel particles in PLA9SS. (c) Spherical and irregular matrix voids in PLA15SS. (d) Comparison of nominal and ImageJ-measured stainless steel content. (e) X-ray diffraction pattern of 316 L stainless steel particles used in the composite formulations. Major diffraction peaks at $2\theta = 43.5°$, 50.7°, and 74.6° correspond to the (111), (200), and (220) crystallographic planes of the austenitic phase, respectively.

most effective stiffness enhancement compared to neat PLA. The ultimate compressive strength reached up to 100 MPa. In contrast to the tensile response, all samples exhibited a clear yield point followed by strain hardening. Among the tested orientations, the 90° raster consistently provided the highest compressive strength, indicating improved load transfer along the build direction.

Although modulus and ultimate strength followed predictable reinforcement and orientation trends, yield strength exhibited

15480569, 0, Downloaded from https://4spepublications.onlinelibrary.wiley.com/doi/10.1002/pc.70888 by Gazi University, Wiley Online Library on [04/02/2026]. See the Terms and Conditions (https://onlinelibrary.wiley.com/terms-and-conditions) on Wiley Online Library for rules of use; OA articles are governed by the applicable Creative Commons License

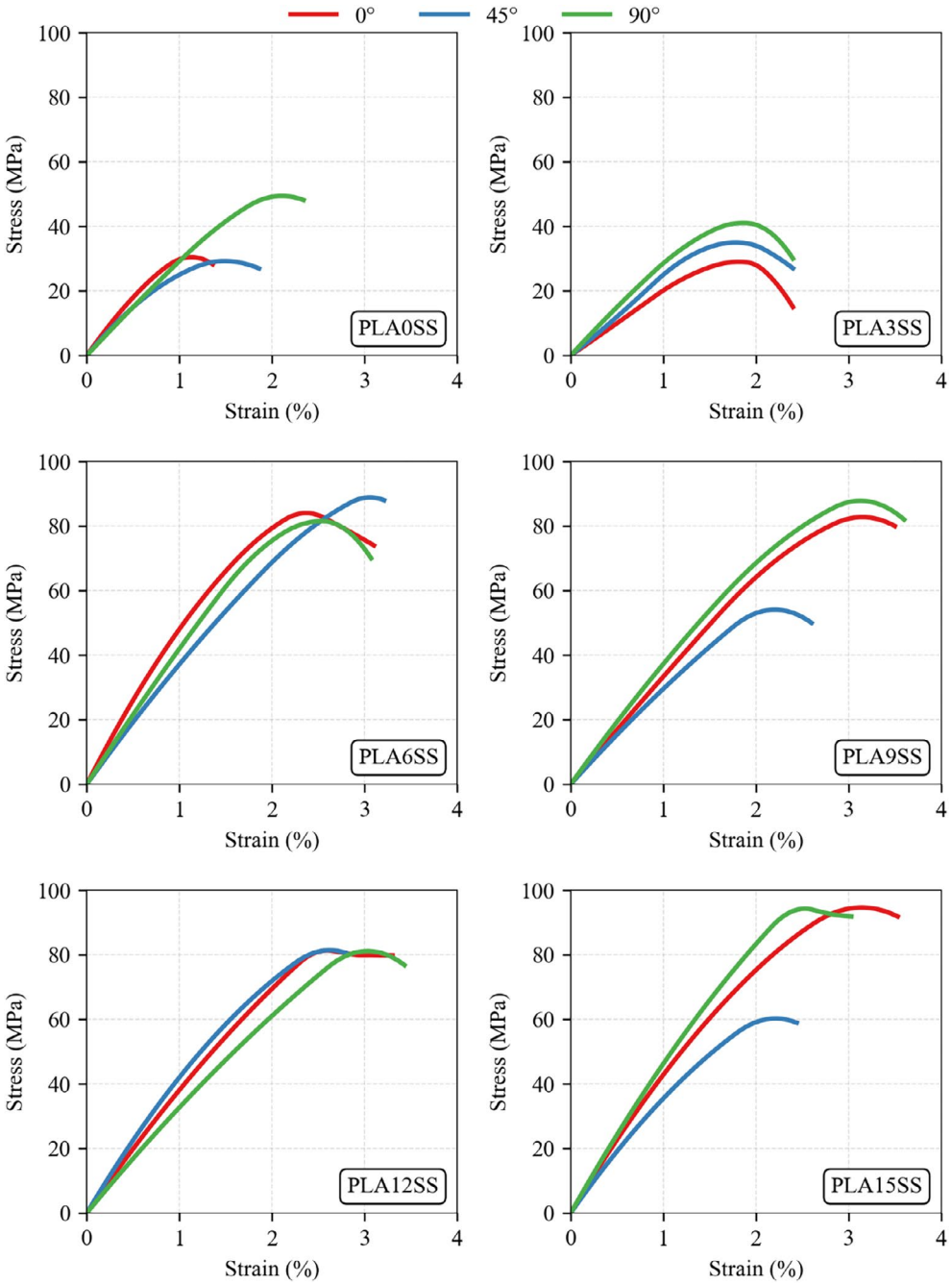


FIGURE 6 | Tensile stress–strain curves of the PLA and PLA-SS composites.

irregular variations. The highest value around 0.45 MPa was recorded for the PLA6SS–90° specimen, indicating improved resistance to initial plastic deformation under compressive loads. Across all groups, strain-to-failure remained relatively uniform, mostly between 5% and 6%, reflecting stable ductility in compression. The superior performance of the 90° orientation is attributed to minimized interlayer delamination and favorable stress distribution along the loading axis.

3.4.3 | Impact Test

(Figure 8) presents the impact energy absorption results for neat PLA and PLA/SS composites tested in accordance with ASTM D6110. The calculated impact strength values (kJ/m^2) were derived based on the ligament area of the notched specimens. Neat PLA specimens exhibited a distinct variation depending on the printing orientation. The 0° orientation yielded the highest impact energy at 0.70 J (35.0 kJ/m^2), whereas the 45° and 90° orientations showed significantly lower values of 0.20 J (10.0 kJ/m^2) and 0.27 J (13.5 kJ/m^2), respectively. Specifically, the 45° orientation demonstrated the lowest resistance among the neat polymer samples.

With the incorporation of SS particles, an initial increase in impact energy was observed. At 3% SS, impact energies rose across all orientations, reaching 0.76 J (38.0 kJ/m^2) for the 0° specimens. A substantial relative increase was noted in the 45° orientation, rising from 0.20 J to 0.50 J. The maximum unidirectional

15480569, 0, Downloaded from https://4spepublications.onlinelibrary.wiley.com/doi/10.1002/pc.70888 by Gazi University, Wiley Online Library on [04/02/2026]. See the Terms and Conditions (https://onlinelibrary.wiley.com/terms-and-conditions) on Wiley Online Library for rules of use; OA articles are governed by the applicable Creative Commons License

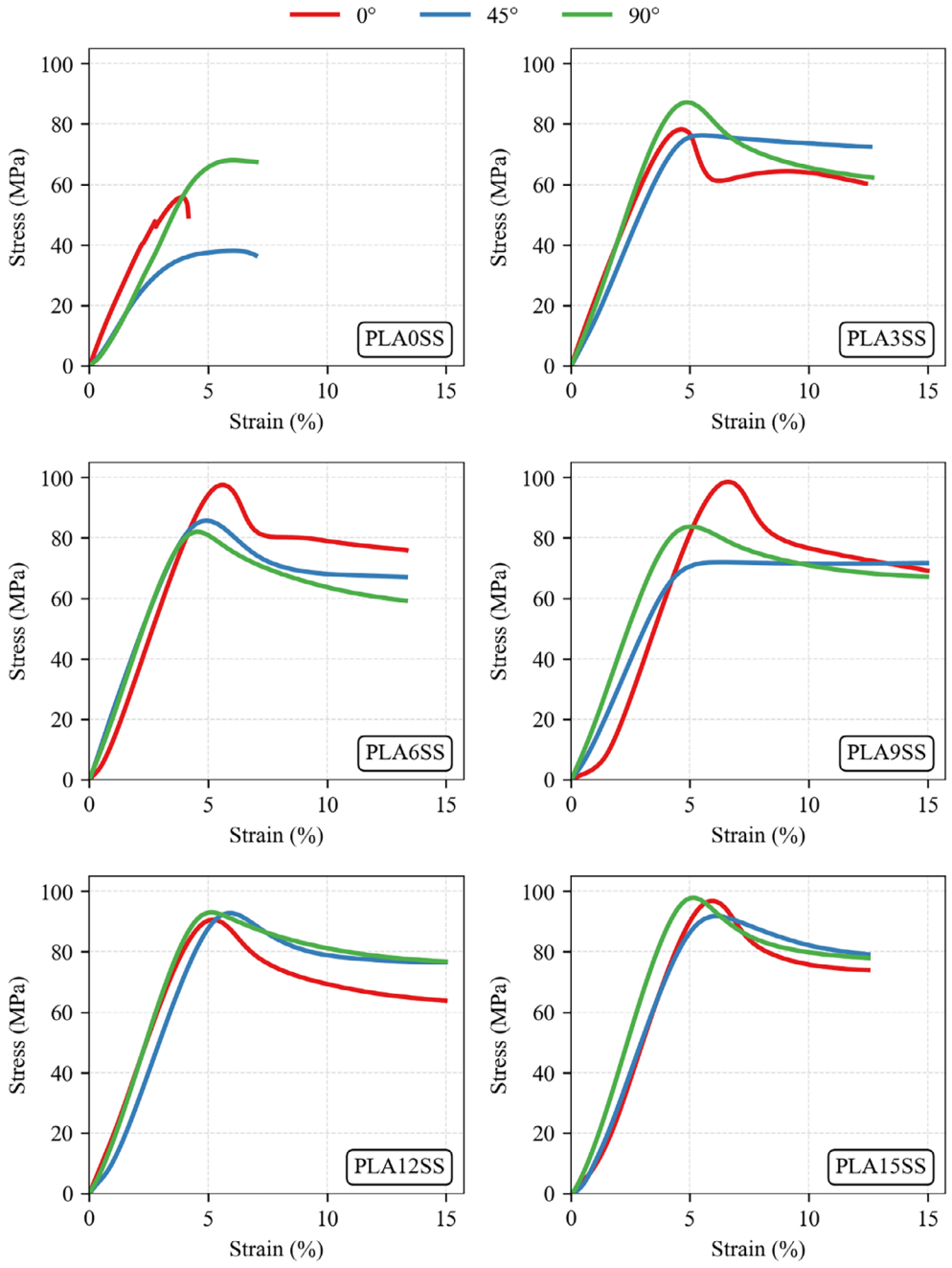


FIGURE 7 | Compressive stress–strain curves by composition and orientation.

impact resistance in this study was recorded at 6% SS for the 0° orientation (0.94 J or 47.0 kJ/m^2). However, a deviation from this increasing trend occurred at 9% SS content, where the impact energy for the 0° and 45° orientations decreased to 0.62 J (31.0 kJ/m^2) and 0.28 J (14.0 kJ/m^2), respectively. In contrast, the 90° orientation at this loading level did not follow the downward trend, exhibiting a value of 0.67 J (33.5 kJ/m^2).

At higher reinforcement contents (12% and 15%), the impact energy values recovered and became notably uniform across different printing directions. At 12% SS, the 0° orientation recovered to 0.85 J, while the 45° orientation reached 0.73 J. Finally, the PLA/15% SS composites displayed the most stable behavior with values of 0.71 J, 0.73 J, and 0.69 J for 0°, 45°, and 90° orientations, respectively.

3.5 | Statistical Optimization and Determination of Optimal Processing Parameters

The influence of processing parameters on the mechanical performance of PLA/SS composites was statistically evaluated using a Taguchi L18 orthogonal array. Four critical parameters (i) SS content (wt.%), (ii) printing orientation (°), (iii) nozzle temperature (°C), and (iv) printing speed (mm/min) were optimized using a hybrid Taguchi–GRA to simultaneously maximize tensile strength (TS), compressive strength (CS), and Charpy impact strength (CIS). The mechanical responses exhibited considerable variability with tensile strength ranging from 28.26 to 94.00 MPa, compressive strength from 39.95 to 98.57 MPa, and impact strength from 0.20 to 0.94 J/cm^2, emphasizing the critical role of parameter selection (Table S1).

15480569, 0, Downloaded from https://4spepublications.onlinelibrary.wiley.com/doi/10.1002/pc.70888 by Gazi University, Wiley Online Library on [04/02/2026]. See the Terms and Conditions (https://onlinelibrary.wiley.com/terms-and-conditions) on Wiley Online Library for rules of use; OA articles are governed by the applicable Creative Commons License

ANOVA results demonstrated that SS content was the primary factor influencing tensile strength, accounting for 80.45% of the total variation (F-value: 57.06, $p < 0.05$). Printing orientation and nozzle temperature showed moderate but statistically significant contributions (~9% each), whereas printing speed had a negligible effect (< 1%). The low error value (1.69%) supports the robustness of the experimental design. Full ANOVA outputs are provided in Table S2.

A similar trend was observed for compressive strength, where SS content remained the dominant parameter (77.72%, $p < 0.05$). Orientation and nozzle temperature contributed moderately (9.44% and 4.22%, respectively), while printing speed had a limited influence (2.54%). The error term (6.21%) remained within acceptable limits, indicating the model's adequacy in explaining compressive performance variability (Table S3).

In the case of impact strength, printing orientation emerged as the leading factor, contributing 39.72% to the total variation. SS content followed with 28.16% influence, while nozzle temperature and print speed had minimal impact. Although p-values for the main factors were slightly above 0.05, the analysis still highlights their potential role. A higher error margin (25.75%) suggests additional variability inherent to impact testing. Complete data are available in Table S4.

A hybrid Taguchi–GRA was employed to identify the optimal combination of process parameters by integrating tensile, compressive, and impact responses into a single gray relational grade (GRG). The ranking of GRG values revealed that SS content had the strongest influence on overall mechanical performance, followed by printing orientation, while nozzle temperature and speed had relatively minor effects. The corresponding values and rankings are presented in Tables S5 and S6, and summarized in (Figure 9).

ANOVA performed on GRG data confirmed these trends statistically, with SS content contributing over 70% to total variability ($p < 0.01$) and printing orientation accounting for approximately 16% ($p < 0.05$). The combined model showed strong explanatory power with an error margin below 9% (see Table S7).

To validate the optimization model, confirmation tests were conducted using the optimal parameter combination (15 wt% SS, 0° orientation, 270 C, 205 mm/min). As shown in Table S8, experimental results closely matched predictions, with errors below 4% and accuracy exceeding 96% across all metrics.

Furthermore, regression equations derived from the experimental data quantitatively express the influence of each process parameter on mechanical properties:

$$\begin{aligned} \textit{Tensile Strength} = & -23.6 + 3.693 \times \text{SS (wt\%)} + 0.0704 \times \text{Orientation} \\ & + 0.2168 \times \text{Nozzle Temp } (^{\circ}\text{C}) \\ & + 0.006 \times \text{Printing Speed (mm/ min)} \end{aligned} \tag{4}$$

$$\begin{aligned} \textit{Compressive Strength} = & 56.5 + 2.230 \times \text{SS (wt\%)} \\ & - 0.0369 \times \text{Orientation} \\ & + 0.1001 \times \text{Nozzle Temp } (^{\circ}\text{C}) \\ & - 0.056 \times \text{Printing Speed (mm/ min)} \end{aligned} \tag{5}$$

$$\begin{aligned} \textit{Charpy Impact Toughness} = & 1.100 + 0.01896 \times \text{SS (wt\%)} \\ & - 0.00319 \times \text{Orientation } (^{\circ}\text{C}) \\ & - 0.00024 \times \text{Nozzle Temp } (^{\circ}\text{C}) \\ & - 0.00210 \times \text{Printing Speed (mm/ min)} \end{aligned} \tag{6}$$

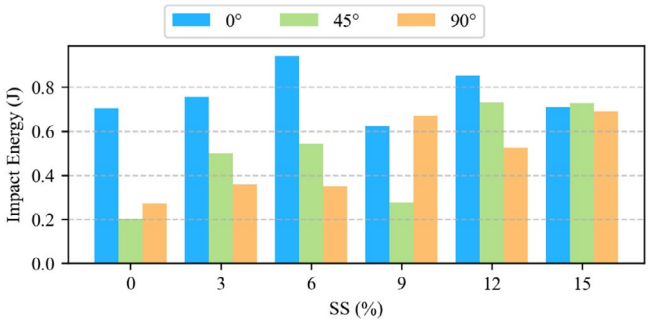


FIGURE 8 | Charpy impact energy for each composite formulation.

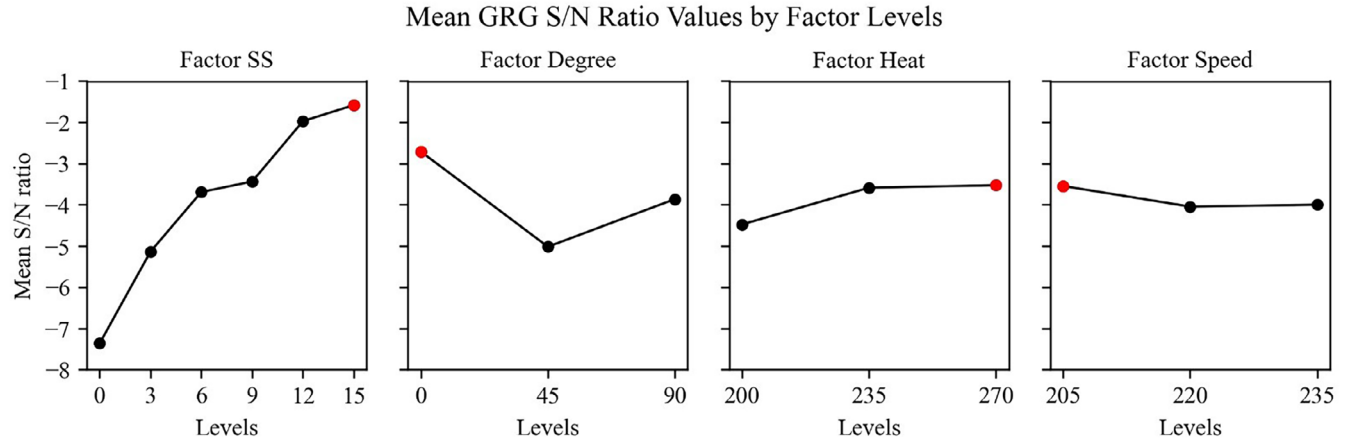


FIGURE 9 | Mean GRG S/N ratio values by factor levels.

15480569, 0, Downloaded from https://4spepublications.onlinelibrary.wiley.com/doi/10.1002/pc.70888 by Gazi University, Wiley Online Library on [04/02/2026]. See the Terms and Conditions (https://onlinelibrary.wiley.com/terms-and-conditions) on Wiley Online Library for rules of use; OA articles are governed by the applicable Creative Commons License

3.6 | Multi-Parameter Optimization Results

Multi-parameter optimization contour plots are presented in (Figure 10), illustrating the interaction effects among the four processing variables on mechanical performance. High GRG response regions (indicated by warmer colors) were primarily associated with combinations of high SS content and low printing orientation. In contrast, nozzle temperature and printing speed had comparatively limited impact on the response surface. The plots visually confirm that the most favorable mechanical performance is achieved at elevated SS content and aligned raster orientation.

3.7 | In Vitro Cytocompatibility

The cytocompatibility of PLA and PLA/316L SS composites was systematically evaluated based on ISO 10993-5 guidelines using extract media obtained after 24 h incubation. Following the addition of extracts to L929 fibroblast cultures, cellular responses were monitored at 24, 48, and 72 h via phase-contrast microscopy.

Microscopic observations demonstrated that all experimental groups, including those with up to 15 wt% stainless steel reinforcement, exhibited confluent and healthy monolayers, with no visible signs of cytotoxicity such as cellular detachment, rounding, or morphological degeneration (Figure 11). In contrast, the negative control group showed significant cell loss and morphological disruption within 72 h. The positive control group maintained high confluency and normal fibroblastic morphology across all time points.

Figure 12 presents the quantitative results of metabolic activity. After 72 h of extract exposure, all PLA/SS composite groups showed viable cell populations comparable to the negative control, with no statistically significant reduction in viable cell number (Figure 12a). The highest cell density was observed in the 3 wt% SS group. Moreover, growth inhibition rates remained below 10% for all composites, confirming the absence of a cytotoxic response (Figure 12b).

Scoring based on ISO 10993-5 evaluation criteria yielded cytotoxic response indices below 1 for all groups, classifying all materials as non-cytotoxic. Together, these findings confirm that the addition of SS up to 15 wt% into PLA matrices does not impair biocompatibility. All tested composites were well tolerated by L929 fibroblast cells, both morphologically and metabolically, validating their cytocompatibility for biomedical use.

4 | Discussion

This study aimed to comprehensively evaluate the influence of stainless steel (316L SS) reinforcement and key fused deposition modeling (FDM) parameters on the mechanical, thermal, microstructural, and cytocompatibility performance of PLA-based biocomposites. By integrating a systematic Taguchi L18 design with GRA, the research not only explored how individual parameters affect material behavior but also identified the optimal processing conditions for maximizing multi-response mechanical performance. The findings presented herein provide critical insight into the feasibility of tailoring PLA/SS composites for load-bearing biomedical applications through process-driven optimization strategies.

4.1 | Thermal and Crystallization Behavior

Thermal analysis revealed that the incorporation of SS particles into PLA induces systematic modifications in the polymer's

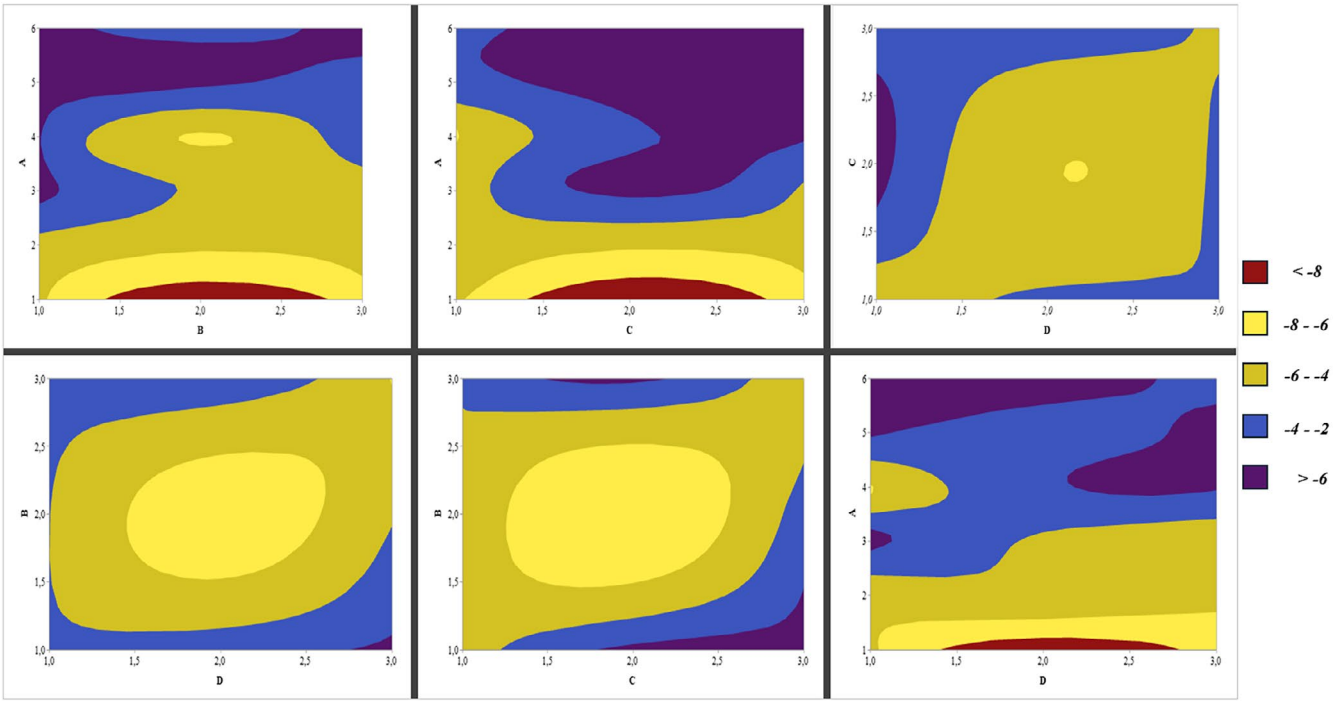


FIGURE 10 | Contour plots illustrating the interactive effects of 316SSL wt.% (A), printing orientation (B), nozzle temperature (C), and printing speed (D) on mechanical performance. Optimal parameter regions are highlighted in yellow, corresponding to the highest response values.

15480569, 0, Downloaded from https://4spepublications.onlinelibrary.wiley.com/doi/10.1002/pc.70888 by Gazi University, Wiley Online Library on [04/02/2026]. See the Terms and Conditions (https://onlinelibrary.wiley.com/terms-and-conditions) on Wiley Online Library for rules of use; OA articles are governed by the applicable Creative Commons License

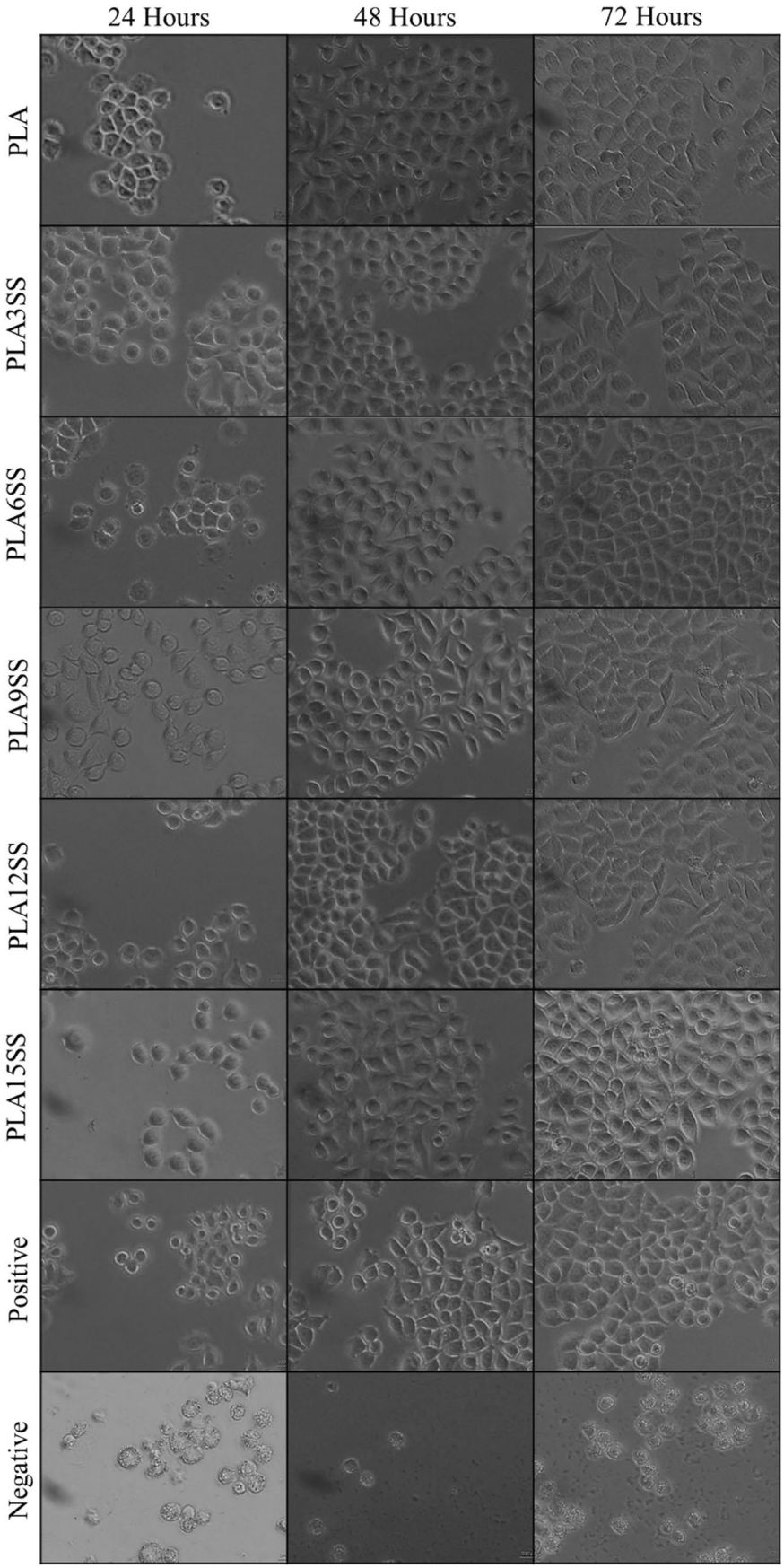


FIGURE 11 | Phase-contrast microscopy images (40×) showing L929 cell morphology at 24, 48, and 72 h after exposure to extract solutions from PLA and PLA/SS composites. All groups displayed healthy, adherent fibroblast morphology. The negative control (−) exhibited severe cytotoxic effects, while the positive control (+) showed high confluency.

15480569, 0, Downloaded from https://4spepublications.onlinelibrary.wiley.com/doi/10.1002/pc.70888 by Gazi University, Wiley Online Library on [04/02/2026]. See the Terms and Conditions (https://onlinelibrary.wiley.com/terms-and-conditions) on Wiley Online Library for rules of use; OA articles are governed by the applicable Creative Commons License

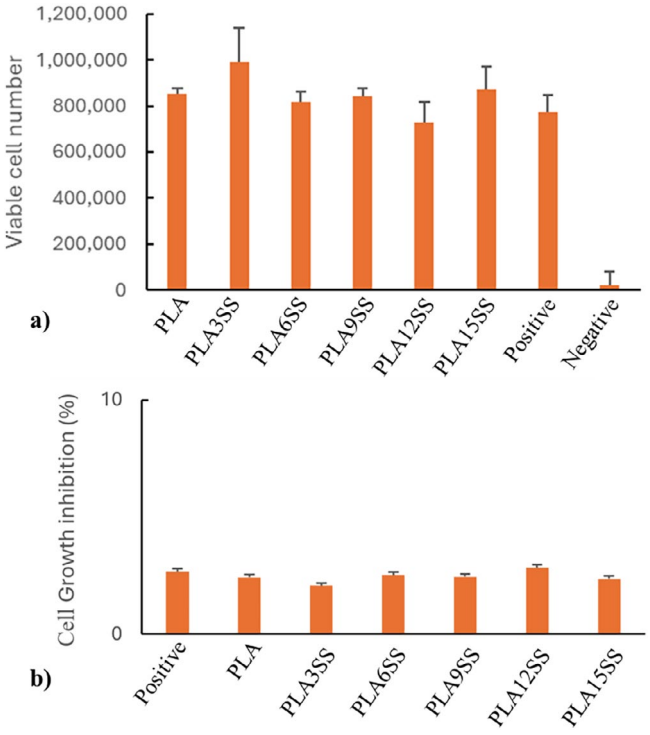


FIGURE 12 | Quantitative cytocompatibility evaluation at 72 h: (a) Viable cell number in response to extract media from PLA and PLA/SS composites. (b) Growth inhibition percentage relative to positive control. All values remained within the non-cytotoxic range.

thermal transitions and stability. As summarized in (Table 4), the glass transition temperature (Tg) increased progressively with increasing SS content, rising from approximately 60°C at 3 wt% SS to about 73°C at 15 wt%. This behavior reflects increasing restrictions on amorphous chain mobility, which can be attributed to enhanced polymer–filler interactions and reduced segmental freedom at higher SS loadings.

Cold crystallization behavior exhibited a strong dependence on filler content. DSC thermograms showed distinct exothermic cold-crystallization features for composites containing 3–9 wt% SS, while the signal weakened considerably at 12 wt% and became barely detectable at 15 wt%. This evolution closely follows the reduction in ΔHcc values reported in (Table 4), indicating that increasing SS content progressively limits the ability of amorphous PLA chains to reorganize into crystalline domains during reheating. The combined effects of filler-induced chain immobilization and geometric confinement imposed by metal particles effectively suppress cold crystallization at higher filler levels.

The degree of crystallinity (Xc), calculated from the enthalpy balance between melting and cold crystallization, remained relatively low across all compositions (≈3%–5%). The small difference between ΔHm and ΔHcc suggests that a substantial portion of the crystalline phase develops during the heating cycle rather than existing as stable crystallites prior to DSC analysis. With increasing SS content, the simultaneous decrease in both ΔHm and ΔHcc reflects an overall inhibition of crystal growth and reorganization, likely caused by steric hindrance and reduced chain mobility in the vicinity of SS particles.

Melting behavior showed only minor variations with filler loading. The melting temperature (Tm), determined from the peak position of the melting endotherm, exhibited a slight decrease from approximately 149°C at 3 wt% SS to about 144°C at 15 wt% SS, while the melting endotherms became progressively broader. This broadening indicates the formation of less perfect and more heterogeneous crystalline structures. Such a reduction in crystallinity is generally considered beneficial for fused deposition modeling (FDM) processing, as it can mitigate warpage and dimensional instability associated with crystallization-induced shrinkage [59]. In contrast, the elevated Tg observed at higher SS loadings suggests improved thermal resistance, which may expand the usable service temperature window of the composites in applications requiring enhanced thermal stability [60].

Thermogravimetric analysis (TGA) was conducted up to 200°C to specifically assess thermal stability under FDM-relevant conditions. The TG and DTG curves showed minimal mass loss (< 0.6%) for all compositions within this temperature range, confirming that neither neat PLA nor the PLA/SS composites undergo significant thermal degradation during processing. A gradual increase in residual mass with increasing SS content was observed and is directly associated with the inert metallic fraction. These results indicate that SS particles can act as effective thermal barriers, slowing heat transfer and the evolution of volatile degradation products, thereby contributing to the thermal stability of the composites [61].

4.2 | Microstructure–Property Relationships

The microstructural analysis of both neat PLA and PLA/SS composite filaments revealed several critical features governing the mechanical performance of additively manufactured specimens. High-magnification imaging showed that all samples, including neat PLA, exhibited elongated striations aligned with the extrusion direction (Figure 5a). These elongated striations, visible under SEM, are a result of molecular chain orientation induced during the filament extrusion process. Such anisotropic patterns were consistent across all formulations, indicating that extrusion dynamics particularly the shear and elongational flow fields during filament formation are the primary drivers of this molecular alignment. The presence of such orientation suggests inherent anisotropy in the microstructure, which directly influences the mechanical behavior of FDM-printed parts, especially in terms of tensile strength, stiffness, and failure mechanisms, depending on the alignment between the filament orientation and the applied load.

At higher SS filler contents, detailed microstructural examination revealed the onset and progression of particle agglomeration and associated porosity (Figure 4b, PLA9SS). Clusters of closely packed SS particles were frequently observed, likely resulting from insufficient shear mixing or inadequate wetting during filament fabrication. These agglomerates serve as mechanical stress concentrators, compromising reinforcement efficiency and promoting localized failure under mechanical load. Two distinct types of cavities were also identified: spherical voids and irregularly shaped pores (Figure 5c, PLA15SS). The spherical voids are attributed to entrapped gas bubbles or

15480569, 0, Downloaded from https://4spepublications.onlinelibrary.wiley.com/doi/10.1002/pc.70888 by Gazi University, Wiley Online Library on [04/02/2026]. See the Terms and Conditions (https://onlinelibrary.wiley.com/terms-and-conditions) on Wiley Online Library for rules of use; OA articles are governed by the applicable Creative Commons License

incomplete matrix filling during extrusion, as their uniform shapes are inconsistent with the irregular geometry of the SS particles. In contrast, the irregular cavities, often observed after polishing and grinding, may result from localized poor polymer flow, shrinkage-induced porosity, or weak particle–matrix interactions. Importantly, no clear evidence of interfacial debonding or particle pull-out was detected.

Optical microscopy conducted along different sectioning planes (normal, longitudinal, and transverse; Figure 4) further confirmed distinct morphological trends associated with SS content. At lower filler loadings, the composites exhibited fine and uniform particle dispersion with minimal microstructural defects. However, as SS content exceeded 6–9 wt%, the progressive development of interlayer micro-defects, pronounced flow lines, increasing particle agglomeration, and periodically aligned interlayer voids became more prominent. The flow lines, likely originating from shear-induced alignment during filament deposition, were increasingly pronounced at higher filler contents, suggesting rising flow instability and reduced matrix mobility. The growing degree of agglomeration and periodic void alignment disrupted interlayer continuity, thereby compromising filament-to-filament adhesion. This transition from homogeneous dispersion to defect-dominated microstructure was particularly evident at 9–15 wt% SS, where the FDM process appeared increasingly sensitive to filler-induced flow irregularities and insufficient interlayer fusion.

These microstructural transitions directly impacted mechanical performance. While SS incorporation aimed to reinforce the composites, excessive filler content combined with processing-induced defects such as voids and interlayer gaps often diminished the expected mechanical benefits. Although higher SS contents theoretically enhance strength and stiffness, poor dispersion and compromised interlayer bonding frequently led to reduced ductility and premature failure [62]. These observations highlight the critical importance of optimizing both filler content and processing parameters to achieve a favorable balance between reinforcement and structural integrity in FDM-printed PLA/SS composites. Furthermore, the XRD results support that the mechanical and thermal responses of the composites primarily originate from particle dispersion and matrix–particle interactions rather than changes in particle crystallinity.

4.3 | Mechanisms Underlying Enhanced Mechanical Properties

The use of an optical strain tracking method during tensile testing significantly improved the accuracy of mechanical characterization by capturing localized deformations within the gauge section. While load cell data generally provide consistent results, traditional strain measurements often suffer from artifacts caused by grip slippage or machine compliance, particularly for small or compliant specimens. The tracking technique effectively isolated true specimen deformation, allowing more precise stress–strain analysis. However, due to geometric constraints and fixture obstructions, this method could not be applied during compression testing of cylindrical specimens [63].

Before interpreting the mechanical test results, it is crucial to emphasize that each data point presented in this study corresponds to a specific combination of process parameters determined by the Taguchi L18 orthogonal array. Although figure legends and textual descriptions frequently refer to SS content and raster orientation alone (e.g., PLA6SS–0°) for brevity, they inherently include a distinct nozzle temperature and printing speed as well (see Table 2). Consequently, the observed mechanical behavior should not be attributed to isolated parameters but rather understood as the result of multifactorial interactions.

Tensile test results showed that neat PLA exhibited the lowest elongation among all tested materials. Interestingly, the tensile performance demonstrated a non-uniform dependence on raster orientation, as peak tensile strengths varied across 0°, 45°, and 90° orientations (Figure 6). This variability suggests that, in addition to raster orientation, processing parameters such as nozzle temperature and print speed also significantly influence mechanical performance [64]. Despite these variations, all reinforced composites exhibited substantially superior mechanical properties compared to neat PLA across all orientations, emphasizing the reinforcing role of SS fillers. The absence of a clear trend highlights the complex interplay between multiple processing factors in determining composite performance.

The superior tensile strength and toughness of PLA/SS composites compared to neat PLA can be primarily attributed to efficient stress transfer mechanisms facilitated by well-dispersed SS particles, as confirmed by optical microscopy, SEM, and EDX analyses [65, 66]. The metallic fillers act as load-bearing elements within the polymer matrix, effectively restricting molecular chain mobility under applied stress. This leads to substantial improvements in both tensile and compressive strengths [44, 67], consistent with reinforcement mechanisms previously reported for PLA-metal composites [40, 68].

As presented in (Figure 8), the Charpy impact test results reveal a strong dependence of neat PLA on printing orientation, confirming the inherent anisotropy of FDM-processed parts. The superior performance of the 0° orientation is attributed to the alignment of filaments perpendicular to the crack propagation path, which maximizes the load-bearing capacity of the polymer chains. Conversely, the lower resistance observed at 45° is likely due to shear stress dominance along the raster lines, facilitating rapid crack growth through the inter-raster interfaces.

The addition of SS reinforcement generally enhanced the energy absorption capacity. The significant improvement observed at 3 wt% SS compared to neat PLA, particularly in the 45° orientation, suggests that the reinforcement particles began to impede crack propagation along the raster interface. Although 6 wt% SS for 0° provided the highest peak impact energy, the material retained its anisotropic character. The reduction in impact energy observed at 9 wt% SS for 0° and 45° orientations may be attributed to localized particle agglomeration. These agglomerates likely acted as stress concentrators rather than reinforcement, initiating premature failure within the matrix. The anomalous behavior of the 90° orientation at this content implies a complex interaction where defects might be less critical when the load is applied parallel to the layer deposition, or it may indicate

15480569, 0, Downloaded from https://4spepublications.onlinelibrary.wiley.com/doi/10.1002/pc.70888 by Gazi University, Wiley Online Library on [04/02/2026]. See the Terms and Conditions (https://onlinelibrary.wiley.com/terms-and-conditions) on Wiley Online Library for rules of use; OA articles are governed by the applicable Creative Commons License

experimental variability common in heterogeneous composites at threshold loading levels.

A key finding of this study is the shift towards isotropy observed at higher reinforcement contents. The convergence of impact energy values at 15 wt% SS implies that at high loading fractions, the mechanical properties are dominated by the metal particulate network rather than the FDM raster pattern. The reinforcement effectively bridges the inter-raster gaps, leading to a homogenized energy dissipation mechanism that is independent of the printing direction.

However, it is important to note that at filler loadings exceeding approximately 9 wt%, increased agglomeration and void formation can become critical, a phenomenon often cited to negatively impact mechanical performance [69]. These microstructural imperfections act as stress concentrators, leading to premature failure, particularly under dynamic loading conditions such as impact tests. SEM and EDX examinations confirmed that higher SS loadings promoted particle agglomeration and increased inter-particle voids, thus reducing the mechanical benefits expected from higher filler contents.

The superior performance of 0° oriented specimens can be explained by the alignment of deposited filaments parallel to the loading direction, minimizing the number of interlayer boundaries that typically represent weak points in FDM structures [30, 70, 71]. Conversely, the enhanced impact resistance at 45° orientation likely results from more favorable crack propagation paths and energy dissipation mechanisms, as cracks must traverse multiple layer interfaces rather than propagating along a single interlayer boundary [71].

A comprehensive analysis of the mechanical performance, supported by the tabular data presented (Table 5), reveals a noteworthy advancement in the properties of PLA/SS biocomposites when compared to neat PLA and several commonly referenced biomaterials. Specifically, the tensile strength results illustrate significant trends across varying 316L SS content, with a pronounced improvement observed at 9 wt% and 12 wt%, where ultimate tensile strength reaches up to 94 MPa, a significant enhancement compared to the 63 MPa measured for pure PLA. This pattern is echoed in compressive strength results, where the composites achieve a maximum value of 101.7 MPa, surpassing values typically reported for both neat PLA and PLA/Ti composites [72], as well as matching or exceeding benchmarks for cortical bone as noted by Farazin et al. [73].

TABLE 5 | Comparison of mechanical properties of the optimized PLA/316L composites with literature values for similar biocomposite systems [78, 79].

Material	UTS (MPa)	CS (MPa)	ES (MPa)
Optimum PLA/SS	94	101.7	3700
Pure PLA	63	73	2400
PLA/Ti	80	88	3500
PEEK	90	110	3800
PMMA	65	90	2800
Cortical Bone	100	155	15,000

The elastic modulus values of optimized PLA/SS composites, reaching up to 3700 MPa, approach the lower boundary of human cortical bone's modulus range (7000–30,000 MPa) [74, 75], highlighting significant improvement over typical PLA-based materials [76, 77] These findings demonstrate acceptable properties over many common biomaterials such as PEEK, PMMA, and other PLA-based composites regarding both strength and modulus (Table 5). Critically, the incorporation of stainless steel fillers effectively enhances mechanical properties while retaining the biodegradable and processability advantages of the PLA matrix. Beyond biomedical applications, these enhanced properties suggest potential uses in non-load-bearing automotive and aerospace components, where lightweight and moderate strength are advantageous. However, due to their modulus still being relatively low compared to traditional structural materials, these composites are not recommended for load-bearing structural applications in critical engineering contexts.

Furthermore, literature underscores the excellent cytocompatibility and corrosion resistance of SS in physiological environments [6, 19], supporting its integration into bioresorbable matrix systems for either temporary or permanent biomedical applications. The combination of 3D-printed customization, mechanical robustness, and controlled degradability suggests these composites as promising candidates for patient-specific bone tissue engineering, trauma fixation devices, and dental implants, among others [6, 11, 29].

Despite these promising results, several limitations must be acknowledged. First, the current study focused primarily on short-term mechanical properties under static and impact loading conditions. For orthopedic applications, long-term fatigue performance and degradation behavior under physiological conditions are equally critical and warrant further investigation [78, 79]. Second, while SS is generally biocompatible, comprehensive in vitro and in vivo studies would be necessary to evaluate cell-material interactions and potential inflammatory responses to the composites [40]. Finally, the observed agglomeration at higher SS loading suggests that alternative compounding or surface modification strategies might further improve particle dispersion and interfacial adhesion, potentially extending the useful range of filler content [69].

4.4 | Implications of Processing Parameters and Optimization Results

The results of this study provide statistically robust insights into how processing parameters control the mechanical performance of FDM-printed PLA/SS composites.

ANOVA and optimization analysis confirmed that SS content is by far the most significant parameter affecting both tensile and compressive properties, contributing over 70%–80% of the variance. This is attributed to the increased load transfer efficiency, improved matrix rigidity, and optimized microstructure provided by dispersed SS particles. However, at very high SS contents, agglomeration and porosity begin to counteract these

15480569, 0, Downloaded from https://4spepublications.onlinelibrary.wiley.com/doi/10.1002/pc.70888 by Gazi University, Wiley Online Library on [04/02/2026]. See the Terms and Conditions (https://onlinelibrary.wiley.com/terms-and-conditions) on Wiley Online Library for rules of use; OA articles are governed by the applicable Creative Commons License

benefits, which is reflected in plateauing or declining toughness values. This observation is consistent with previous studies on metal-filled polymers.

Impact strength was primarily governed by printing orientation, which explains 40% of the variance in impact behavior. This anisotropy is characteristic of FDM processes, where interlayer adhesion and filament alignment can be strategically exploited to maximize energy absorption and resistance to crack propagation. Within the tested ranges, nozzle temperature and speed were secondary factors, exerting only minor effects on static mechanical properties but having some influence on dynamic behavior. This aligns with literature showing their effects become pronounced only at extreme settings.

The regression models quantitatively demonstrate the positive linear relationship between SS content and all measured properties, supporting the physical mechanisms identified. The close agreement between predicted and experimental values in confirmation runs further validates the model's predictive power.

The optimized processing conditions (15 wt% SS, 0° orientation, 270°C, 205 mm/min) provide a scientifically grounded guideline for manufacturing high-performance PLA/SS composites. The mechanical properties approach those of human cortical bone and surpass many common biomaterials in strength and modulus, making these composites suitable for non-load-bearing biomedical, automotive, and aerospace applications that benefit from lightweight, customizable polymer–metal systems. However, the modulus and absolute strength remain lower than those required for critical structural applications, so their use in primary load-bearing roles is not recommended [80].

Despite robust optimization, the error term in impact testing suggests that other microstructural or process-induced factors (such as residual stress, particle-matrix interface, or thermal history) may also play important roles. Future work should explore these aspects, as well as long-term mechanical durability and degradation in relevant environments.

4.5 | Cytocompatibility and Biomedical Relevance

Extract-based ISO 10993-5 testing with L929 fibroblasts indicates that incorporating 316L stainless steel up to 15 wt% does not induce acute cytotoxicity in PLA matrices over 72 h. The composite groups maintained healthy, confluent monolayers and showed no statistically significant reduction in viable cell number, with growth-inhibition $<10\%$ and cytotoxic response indices <1. These outcomes demonstrate that the mechanical gains achieved through SS reinforcement and FDM parameter optimization can be realized without compromising short-term cytocompatibility.

Mechanistically, the benign cellular response is consistent with limited ionic exposure from 316L SS, whose passive film is inherently stable, and with the physical encapsulation of particles within the PLA matrix. The slightly higher cell density observed at 3 wt% SS may reflect subtle filler-induced changes in surface wettability and protein adsorption or normal experimental variability; in any case, no adverse trend emerged with increasing filler content up to 15 wt%.

These findings strengthen the case for PLA/SS composites in non-load-bearing or load-sharing biomedical uses where form-fit customization, moderate stiffness, and biocompatibility are prioritized. In particular, the conjunction of improved mechanical performance and preserved cytocompatibility supports applications such as patient-specific surgical guides, temporary spacers, splints/casts, dental and cranio-maxillofacial auxiliaries, and external device components manufactured via FDM.

Several boundaries of inference remain. The present evidence derives from short-term, indirect extract assays in a single fibroblast line; it does not capture direct cell–material interactions on as-printed surfaces, immune responses, or long-term degradation/ion-release under physiological or tribocorrosive conditions. Future work should therefore include (i) direct-contact assays with relevant cell types (e.g., osteoblast-like cells, MSCs) and macrophage polarization readouts; (ii) extended extractions under dynamic flow with quantitative metal-ion release; (iii) testing under simulated physiological and tribocorrosive environments with cyclic loading; (iv) bacterial adhesion/biofilm assessments; and (v) evaluation of sterilization-cycle stability and surface-finish effects. Addressing these aspects will be critical to translate the demonstrated cytocompatibility into validated safety for intended, patient-specific clinical use.

4.6 | Practical Implications and Future Prospects

The findings of this study suggest that PLA/316L stainless-steel biocomposites hold practical potential in modern biomedical manufacturing, particularly for patient-specific surgical guides, dental modeling components, protective splints, and temporary orthopedic devices where moderate mechanical strength and cytocompatibility are required. Currently used materials—such as PEEK, PMMA, PA-based polymers, pure PLA, and metallic prototypes—each present limitations including high stiffness and stress shielding in metals, cost and processing constraints in high-performance polymers, and unpredictable degradation behavior in bioabsorbable PLA/PGA systems [81–89]. By contrast, the enhanced mechanical stability and printability demonstrated in this work indicate that metal-filled PLA systems may serve as a practical intermediate option between conventional polymers and metallic devices.

With the increasing adoption of additive manufacturing in surgical planning and early-stage device development, composite materials offering improved mechanical performance while remaining compatible with low-cost fabrication workflows have attracted growing attention. Recent studies report an increasing use of polymer–metal composites in anatomical models, splints, and preoperative devices, particularly in research-driven and early-stage clinical settings [81, 82, 90, 91]. *n* this context, PLA/316L stainless steel composites have been investigated as an alternative material system due to their enhanced stiffness relative to neat PLA, acceptable cytocompatibility, and suitability for fused deposition modeling. These characteristics support

15480569, 0, Downloaded from https://4spepublications.onlinelibrary.wiley.com/doi/10.1002/pc.70888 by Gazi University, Wiley Online Library on [04/02/2026]. See the Terms and Conditions (https://onlinelibrary.wiley.com/terms-and-conditions) on Wiley Online Library for rules of use; OA articles are governed by the applicable Creative Commons License

their use alongside conventional PLA- and PMMA-based materials in applications where moderate mechanical demands and cost efficiency are prioritized, without the need for fully dense metal additive manufacturing.

Overall, these observations place PLA/316L stainless steel composites within the current spectrum of biomedical material systems investigated for additively manufactured devices. Their reported mechanical reinforcement, processability using fused deposition modeling, and cost efficiency support their consideration for early-stage device development and temporary orthopedic applications where patient-specific customization and moderate load-bearing requirements are emphasized.

5 | Conclusions

This study aimed to evaluate and optimize the mechanical, thermal, microstructural, and short-term cytocompatibility performance of FDM-printed PLA/316L SS biocomposites as a function of reinforcement ratio and key printing parameters. By combining melt compounding, filament extrusion, and a Taguchi L18 design with GRA, we established clear process–structure–property relationships and identified an experimentally validated optimum parameter set.

PLA/SS composites containing 0–15 wt% SS were successfully fabricated into dimensionally stable filaments and printed without processing instabilities. SS incorporation led to marked mechanical reinforcement: under the optimal condition (15 wt% SS, 0° raster orientation, 270°C nozzle temperature, 205 mm/s), tensile strength, compressive strength, and elastic modulus increased by approximately 49.2%, 55.7%, and 69.8%, respectively, relative to neat PLA. Taguchi–GRA analysis confirmed SS content as the dominant factor controlling tensile and compressive responses, with build orientation as the second most influential parameter, while nozzle temperature and printing speed played secondary roles. Confirmation experiments performed at the predicted optimum showed excellent agreement with the model, with deviations below 4%, thereby validating the robustness of the optimization approach and the reliability of the resulting property predictions.

Thermal and microstructural characterization demonstrated that SS particles significantly modify PLA's crystallization behavior and morphology. Increasing SS content produced a non-monotonic increase in glass transition temperature and a pronounced decrease in crystallinity (from 21.4% in neat PLA to ~7% at 15 wt% SS), consistent with filler-induced constraints on chain mobility and crystal growth. Microstructural analyses revealed homogeneous particle dispersion and limited defect content at low and intermediate filler levels, whereas higher loadings promoted agglomeration and interlayer voids, rationalizing the observed saturation or decline in mechanical gains at the upper reinforcement range. Within the FDM-relevant temperature window (< 200°C), all formulations exhibited excellent thermal stability.

In vitro cytocompatibility tests (ISO 10993-5, L929 fibroblasts) showed cell viability values exceeding 90% for all composites, indicating that SS reinforcement up to 15 wt% does not induce acute cytotoxicity under the tested conditions. Thus, the mechanical improvements achieved through SS filling and process optimization are obtained without compromising short-term biocompatibility.

Collectively, these findings demonstrate that SS-reinforced PLA produced via FDM can be rationally optimized to deliver substantially enhanced mechanical performance, tunable thermal and microstructural characteristics, and preserved cytocompatibility. The optimized PLA/SS biocomposites approach the lower bound of cortical bone strength while remaining within the stiffness range of polymer-based biomaterials, making them promising candidates for patient-specific, non-load-bearing or load-sharing biomedical components such as surgical guides, protective housings, dental and cranio-maxillofacial prototypes, and preliminary orthopedic aids. Future work should address long-term fatigue and degradation behavior under physiological conditions, extended in vitro/in vivo biocompatibility, and potential surface modification strategies to further refine particle dispersion and interfacial bonding, thereby extending the design space for clinically relevant applications.

Author Contributions

İbrahim Baki Sahin: conceptualization, investigation, methodology, formal analysis, visualization, funding acquisition. **Bayram Sercan Bayram:** conceptualization, investigation, funding acquisition, visualization, methodology, formal analysis, software. **Begum Pinarbasi:** methodology, validation, visualization, writing – original draft. **Pınar Yilgor:** methodology, validation, visualization, writing – original draft. **İhsan Korkut:** supervision, resources, funding acquisition, writing – review and editing, conceptualization, project administration, validation. **Berzah Yavuzyegit:** conceptualization, investigation, methodology, software, data curation, supervision, formal analysis, visualization, funding acquisition, writing – review and editing, writing – original draft.

Acknowledgments

The authors would like to thank the Gazi University Scientific Research Projects Coordination Unit for their support (Project code: FKA-2024-9628).

Funding

This work was supported by Gazi University (Project code: FKA-2024-9628).

Conflicts of Interest

The authors declare no conflicts of interest.

Data Availability Statement

The authors have nothing to report.

References

1. S. Farah, D. G. Anderson, and R. Langer, "Physical and Mechanical Properties of PLA, and Their Functions in Widespread Applications—A Comprehensive Review," *Advanced Drug Delivery Reviews* 107 (2016): 367–392.

2. E. H. Baran and H. Y. Erbil, "Surface Modification of 3D-Printed PLA Objects Produced by Fused Deposition Modeling: A Review," *Colloids and Interfaces* 3, no. 2 (2019): 43.

15480569, 0, Downloaded from https://4spepublications.onlinelibrary.wiley.com/doi/10.1002/pc.70888 by Gazi University, Wiley Online Library on [04/02/2026]. See the Terms and Conditions (https://onlinelibrary.wiley.com/terms-and-conditions) on Wiley Online Library for rules of use; OA articles are governed by the applicable Creative Commons License

3. Z. U. Arif, M. Y. Khalid, R. Noroozi, A. Sadeghianmaryan, M. Jalalvand, and M. Hossain, "Recent Advances in 3D-Printed Polylactide and Polycaprolactone-Based Biomaterials for Tissue Engineering Applications," *International Journal of Biological Macromolecules* 218 (2022): 930–968.

4. J. Domínguez-Robles, N. K. Martin, M. L. Fong, et al., "Antioxidant PLA Composites Containing Lignin for 3D Printing Applications: A Potential Material for Healthcare Applications," *Pharmaceutics* 11, no. 4 (2019): 165.

5. S. N. Figueiredo, A. R. de Oliveira Dias, L. V. Leitão, et al., "Development of Graphite-Reinforced PLA/PBAT Composite Filaments," *Polymer Composites* 46 (2025): 13677–13689.

6. T. Khan, G. Vadivel, B. Ramasamy, G. Murugesan, and T. A. Sebaey, "Biodegradable Conducting Polymer-Based Composites for Biomedical Applications—A Review," *Polymers* 16, no. 11 (2024): 1533.

7. N. G. Khouri, J. O. Bahú, C. Blanco-Llamero, P. Severino, V. O. C. Concha, and E. B. Souto, "Polylactic Acid (PLA): Properties, Synthesis, and Biomedical Applications—A Review of the Literature," *Journal of Molecular Structure* 1309 (2024): 138243.

8. M. Zarei, M. Shabani Dargah, M. Hasanzadeh Azar, et al., "Enhanced Bone Tissue Regeneration Using a 3D-Printed Poly(Lactic Acid)/Ti6Al4V Composite Scaffold With Plasma-Treatment Modification," *Scientific Reports* 13, no. 1 (2023): 3139.

9. R. Baptista and M. Guedes, "Morphological and Mechanical Characterization of 3D-Printed PLA Scaffolds With Controlled Porosity for Trabecular Bone Tissue Replacement," *Materials Science & Engineering, C: Materials for Biological Applications* 118 (2021): 111528.

10. L. F. Velásquez-García and Y. Kornbluth, "Biomedical Applications of Metal 3D Printing," *Annual Review of Biomedical Engineering* 23 (2021): 307–338.

11. E. Zarrabeitia-Bilbao, I. Álvarez-Meaza, R. M. Río-Belver, and G. Garechana-Anacabe, "Additive Manufacturing Technologies for Biomedical Engineering Applications: Research Trends and Scientific Impact," *El Profesional de La Información* 28, no. 2 (2019): 121–139.

12. D. Veeman, M. S. Sai, P. Sureshkumar, et al., "Additive Manufacturing of Biopolymers for Tissue Engineering and Regenerative Medicine: An Overview, Potential Applications, Advancements, and Trends," *International Journal of Polymeric Science* 2021 (2021): 4907027.

13. S. Zhang, X. Chen, M. Shan, et al., "Convergence of 3D Bioprinting and Nanotechnology in Tissue Engineering Scaffolds," *Biomimetics* 8, no. 1 (2023): 94.

14. M. Li, W. Lei, and W. Yu, "FDM 3D Printing and Properties of WF/PBAT/PLA Composites," *Molecules* 29, no. 21 (2024): 5087.

15. C. Pereira-Lobato, M. Echeverry-Rendón, J. P. Fernández-Blázquez, J. Llorca, and C. González, "PLA/PCL Composites Manufactured From Commingled Yarns for Biomedical Applications," *Journal of the Mechanical Behavior of Biomedical Materials* 163 (2025): 106819.

16. K. E. Min, J. W. Jang, C. Kim, and S. Yi, "Enhancement of Mechanical Properties of PCL/PLA/DMSO2 Composites for Bone Tissue Engineering," *Applied Sciences* 14, no. 14 (2024): 6190.

17. P. Senthamaraikannan, "Optimization of Tensile Properties of Melt-Processed Polylactic Acid/*Cissus quadrangularis* Fiber Composites," *Polymer Composites* 47 (2025): 70641.

18. J. Brackett, D. Cauthen, J. Condon, et al., "The Impact of Infill Percentage and Layer Height in Small-Scale Material Extrusion on Porosity and Tensile Properties," *Additive Manufacturing* 58 (2022): 103063.

19. J. Kechagias, D. Chaidas, N. Vidakis, K. Salonitis, and N. M. Vaxevanidis, "Key Parameters Controlling Surface Quality and Dimensional Accuracy: A Critical Review of the Fused-Filament Fabrication Process," *Materials and Manufacturing Processes* 37, no. 9 (2022): 963–984.

20. J. D. Kechagias, S. P. Zaoutsos, D. Chaidas, and N. Vidakis, "Multi-Parameter Optimization of PLA/Coconut Wood Compound for Fused-Filament Fabrication Using Robust Design," *International Journal of Advanced Manufacturing Technology* 119, no. 7 (2022): 4317–4328.

21. B. M. Campos, G. Fontaine, S. Bourbigot, G. Stoclet, and F. Bonnet, "Poly (L-Lactide-Co-ε-Caprolactone)/Glass Fiber Composites: Toward Improved Mechanical Properties of Polylactide-Based Composites," *Polymer Composites* (2025): 70652.

22. H. Sun, W. Luo, Y. Weng, and C. Zhang, "Advances in Poly (Lactic Acid) Chain Extenders: Mechanisms, Performance, and Sustainability," *Journal of Vinyl & Additive Technology* 31 (2025): 67–88.

23. B. L. Martz, T. S. Lee, and G. E. Wnek, "Mechanical Enhancement of Biaxially Cold-Rolled Poly(L-Lactic Acid): Influence of Crystallinity and Short-Term Physical Aging," *SPE Polymers* 6, no. 4 (2025): e70024.

24. M. Faghani, "3D Printing of Hemp-Reinforced Polylactic Acid and Acrylonitrile Styrene Acrylate Filaments: Mechanical Strength Evaluation," *Polymer Composites* (2025): 70564.

25. S. Sharma, P. Sudhakara, J. Singh, R. A. Ilyas, M. R. M. Asyraf, and M. R. Razman, "Critical Review of Biodegradable and Bioactive Polymer Composites for Bone Tissue Engineering and Drug Delivery Applications," *Polymers* 13, no. 16 (2021): 2623.

26. S. Sultan, N. Thomas, M. Varghese, et al., "The Design of 3D-Printed Polylactic Acid–Bioglass Composite Scaffold: A Potential Implant Material for Bone Tissue Engineering," *Molecules* 27, no. 21 (2022): 7214.

27. S. F. Wang, Y. C. Wu, Y. C. Cheng, and W. W. Hu, "The Development of Polylactic Acid/Multi-Wall Carbon Nanotubes/Polyethylene Glycol Scaffolds for Bone Tissue Regeneration Application," *Polymers* 13, no. 11 (2021): 1740.

28. S. Ghasemi, R. Behrooz, I. Ghasemi, R. S. Yassar, and F. Long, "Development of Nanocellulose-Reinforced PLA Nanocomposite Using Maleated PLA (PLA-g-MA)," *Journal of Thermoplastic Composite Materials* 31, no. 8 (2018): 1090–1101.

29. C. Shuai, W. Guo, P. Wu, et al., "A Graphene Oxide–Ag Co-Dispersing Nanosystem: Dual Synergistic Effects on Antibacterial Activities and Mechanical Properties of Polymer Scaffolds," *Chemical Engineering Journal* 347 (2018): 322–333.

30. H. Mei, Z. Ali, Y. Yan, I. Ali, and L. Cheng, "Influence of Mixed Isotropic fiber Angles and Hot Pressing on the Mechanical Properties of 3D-Printed Composites," *Additive Manufacturing* 27 (2019): 150–158.

31. Q. Dong, L. C. Chow, T. Wang, et al., "A New Bioactive Polylactide-Based Composite With High Mechanical Strength," *Colloids and Surfaces A: Physicochemical and Engineering Aspects* 457 (2014): 256–262.

32. V. Chaudhary, C. Ahlawat, B. Sharma, and R. Sahu, "Biodegradation and Characterization of 3D-Printed PLA-Based Polymer Composites Reinforced With Cellulose-Based Hemp/Kenaf Fibers and Coconut/Walnut Fillers," *Polymer Composites* (2025): 1–11.

33. S. Hassanajili, A. Karami-Pour, A. Oryan, and T. Talaei-Khozani, "Preparation and Characterization of PLA/PCL/HA Composite Scaffolds Using Indirect 3D Printing for Bone Tissue Engineering," *Materials Science and Engineering C* 104 (2019): 109960.

34. H. Jeong, J. Rho, J. Y. Shin, D. Y. Lee, T. Hwang, and K. J. Kim, "Mechanical Properties and Cytotoxicity of PLA/PCL Films," *Biomedical Engineering Letters* 8 (2018): 267–272.

35. M. Eryildiz, A. Karakus, and M. E. Altan, "Multifunctional Property Analysis of 3D-Printed Composite Scaffolds From PLA/PCL Filaments With Graphene Oxide Reinforcement," *Polymer Composites* 46 (2025): S804–S818.

36. R. Banupriya, T. P. Jeevan, H. V. Divya, T. G. Yashas Gowda, and G. A. Manjunath, "3D-Printed Graphene-Reinforced Composites: Opportunities and Challenges," *Polymer Composites* 46, no. 2 (2025): 1250–1266.

15480569, 0, Downloaded from https://4spepublications.onlinelibrary.wiley.com/doi/10.1002/pc.70888 by Gazi University, Wiley Online Library on [04/02/2026]. See the Terms and Conditions (https://onlinelibrary.wiley.com/terms-and-conditions) on Wiley Online Library for rules of use; OA articles are governed by the applicable Creative Commons License

37. H. H. Noor and K. F. Alqosaibi, "Investigating the Electrical, Thermal, and Mechanical Properties of 3D-Printed PLA/Talc/Graphene Composites Using the Taguchi Method and Gray Relational Grade Analysis," *Journal of Vinyl and Additive Technology* 31 (2025): 1–13.

38. M. Kalayci and A. B. Irez, "Development of Hybrid Polymer Composites for Electronic Warfare Casings and Investigation of Electromagnetic Interference Shielding Performance," *Polymer Composites* (2025): 1–12.

39. M. Asrofi, M. Rafid, R. R. Pradiza, et al., "Mechanical and Physical Properties of PLA Biocomposites Reinforced With Hybrid Fibers Derived From Cocoa Pod Husk and Dragon Fruit Root for Flexible Packaging," *Journal of Vinyl and Additive Technology* 31, no. 5 (2025): 975–984.

40. M. M. Zerankeshi, R. Bakhshi, and R. Alizadeh, "Polymer/Metal Composite 3D Porous Bone Tissue Engineering Scaffolds Fabricated by Additive Manufacturing Techniques: A Review," *Bioprinting* 25 (2022): e00191.

41. K. Pušnik Črešnar, A. Aulova, D. N. Bikiaris, D. Lambropoulou, K. Kuzmič, and L. Fras Zemljič, "Incorporation of Metal-Based Nanoadditives Into the PLA Matrix: Effect of Surface Properties on Antibacterial Activity and Mechanical Performance of PLA Nanoadditive Films," *Molecules* 26, no. 14 (2021): 4161.

42. X. Zhang, L. Chen, T. Mulholland, and T. A. Osswald, "Characterization of Mechanical Properties and Fracture Mode of PLA and Copper/PLA Composite Parts Manufactured by Fused Deposition Modeling," *SN Applied Sciences* 1, no. 6 (2019): 616.

43. İ. B. Şahin, I. Korkut, L. Urtekin, and B. Yavuzyegit, "Recent Advances in Metal Particle–Reinforced Polylactic Acid Biocomposites via Additive Manufacturing for Biomedical Applications," *Arabian Journal for Science and Engineering* 50 (2025): 1–41.

44. J. Lee, H. Lee, K. H. Cheon, et al., "Fabrication of Poly(Lactic Acid)/titanium Composite Scaffolds With Enhanced Mechanical Properties and Biocompatibility via Fused Filament Fabrication–Based 3D Printing," *Additive Manufacturing* 30 (2019): 100883, https://doi.org/10.1016/j.addma.2019.100883.

45. D. Jiang, F. Ning, and Y. Wang, "Additive Manufacturing of Biodegradable iron-Based Particle–Reinforced Polylactic Acid Composite Scaffolds for Tissue Engineering," *Journal of Materials Processing Technology* 289 (2021): 116952, https://doi.org/10.1016/j.jmatprotec.2020.116952.

46. G. Wang, D. Zhang, G. Wan, B. Li, and G. Zhao, "Glass fiber–Reinforced PLA Composite With Enhanced Mechanical Properties, Thermal Behavior, and Foaming Ability," *Polymer* 181 (2019): 121803, https://doi.org/10.1016/j.polymer.2019.121803.

47. N. Somsuk, S. Pramoonmak, B. Chongkolnee, P. Tipboonsri, and A. Memon, "Enhancing Mechanical Properties of 3D-Printed PLA Composites Reinforced With Natural Fibers: A Comparative Study," *Journal of Composites Science* 9, no. 4 (2025): 180.

48. A. K. Trivedi and M. K. Gupta, "PLA-Based Biodegradable Bionanocomposite Filaments Reinforced With Nanocellulose: Development and Analysis of Properties," *Scientific Reports* 14 (2024): 23819.

49. A. Thirugnanasamabandam, M. Subramaniyan, B. Prabhu, and K. Ramachandran, "Development and Comprehensive Investigation of PLA/Carbon fiber–Reinforced PLA-Based Structurally Alternate Layered Polymer Composites," *Journal of Industrial and Engineering Chemistry* 136 (2024): 248–257, https://doi.org/10.1016/j.jiec.2024.02.012.

50. G. M. Khalid and N. Billa, "Solid Dispersion Formulations by Fused Deposition Modeling 3D Printing—A Review," *Pharmaceutics* 14, no. 4 (2022): 690.

51. C. Vaida, G. Pop, P. Tucan, B. Gherman, and D. Pisla, "Multi-Parametric Optimization of 3D-Printed Components," *Polymers* 17, no. 1 (2024): 27.

52. J. Pohjola, T. Soukka, M. Jokinen, and M. Stolt, "Material Extrusion 3D Printing With Polymer Microsphere Inks: Effects of Solid Volume Fraction and Extrudate Swell on the Resolution and Suitable Processing Parameters," *CIRP Journal of Manufacturing Science and Technology* 60 (2025): 182–194, https://doi.org/10.1016/j.cirpj.2025.05.002.

53. C. Zhai, "A Review on Process Parameter Influence and Optimization for 3D Printing of Fiber-Reinforced Thermoplastic Composites," *Journal of Reinforced Plastics and Composites* 82 (2024): 07316844241273038.

54. S. Chen, L. Cai, Y. Duan, X. Jing, C. Zhang, and F. Xie, "Performance Enhancement of 3D-Printed Carbon fiber–Reinforced Nylon-6 Composites," *Polymer Composites* 45, no. 6 (2024): 5754–5772.

55. M. Rizwee and D. Kumar, "Optimizing Mechanical Behaviour of Polylactic Acid (PLA) Specimen in Fused Deposition Modeling (FDM): A Taguchi Approach. Progress in Rubber," *Plastics and Recycling Technology* 42, no. 1 (2024): 62–83, https://doi.org/10.1177/14777606241306462.

56. H. Schreier, J. J. Orteu, and M. A. Sutton, *Image Correlation for Shape, Motion and Deformation Measurements: Basic Concepts, Theory and Applications* (Springer US, 2009).

57. B. Pan, K. Qian, H. Xie, and A. Asundi, "Two-Dimensional Digital Image Correlation for In-Plane Displacement and Strain Measurement: A Review," *Measurement Science and Technology* 20, no. 6 (2009): 062001.

58. J. Hebert and M. Khonsari, "The Application of Digital Image Correlation in Fatigue Experimentation: A Review," *Fatigue and Fracture of Engineering Materials and Structures* 46, no. 4 (2023): 1256–1299.

59. A. Antony Samy, A. Golbang, E. Harkin-Jones, E. Archer, M. Dahale, and A. McIlhagger, "Influence of Ambient Temperature on Part Distortion: A Simulation Study on Amorphous and Semi-Crystalline Polymers," *Polymers* 14, no. 5 (2022): 879.

60. J. Jin, Y. Su, J. Guo, et al., "Flexible Composite Films With Ultrahigh Through-Plane Thermal Conductivity Yet Low Graphene Content," *Composites Part B: Engineering* 286 (2024): 111780.

61. G. Gałko and M. Sajdak, "Trends for the Thermal Degradation of Polymeric Materials: Analysis of Available Techniques, Issues, and Opportunities," *Applied Sciences* 12, no. 18 (2022): 9138.

62. O. Folorunso, Y. Hamam, R. Sadiku, and W. Kupolati, "Effects of Defects on the Properties of Polymer Nanocomposites: A Brief Review," *Journal of Inorganic and Organometallic Polymers and Materials* 34, no. 12 (2024): 5667–5690.

63. X. Zhang, K. Guan, J. Zhong, G. Chen, W. Wang, and Q. Wang, "A Macro-Pillar Compression Technique for Determining True Stress–Strain Curves of Steels," *Measurement* 168 (2021): 108407.

64. T. Gajjar, R. Yang, L. Ye, and Y. X. Zhang, "Effects of Key Process Parameters on Tensile Properties and Interlayer Bonding Behavior of 3D-Printed PLA Using Fused Filament Fabrication," *Progress in Additive Manufacturing* 10, no. 2 (2025): 1261–1280.

65. A. Dey and N. Yodo, "A Systematic Survey of FDM Process Parameter Optimization and Their Influence on Part Characteristics," *Journal of Manufacturing And Materials Processing* 3, no. 3 (2019): 64, https://doi.org/10.3390/jmmp3030064.

66. J. M. Chacón, M. A. Caminero, E. García-Plaza, and P. J. Núñez, "Additive Manufacturing of PLA Structures Using Fused Deposition Modelling: Effect of Process Parameters on Mechanical Properties and Their Optimal Selection," *Materials & Design* 124 (2017): 143–157, https://doi.org/10.1016/j.matdes.2017.03.065.

67. V. S. Vakharia, L. Kuentz, A. Salem, M. C. Halbig, J. A. Salem, and M. Singh, "Additive Manufacturing and Characterization of Metal Particulate Reinforced Polylactic Acid (PLA) Polymer Composites," *Polymers* 13, no. 20 (2021): 3545.

15480569, 0, Downloaded from https://4spepublications.onlinelibrary.wiley.com/doi/10.1002/pc.70888 by Gazi University, Wiley Online Library on [04/02/2026]. See the Terms and Conditions (https://onlinelibrary.wiley.com/terms-and-conditions) on Wiley Online Library for rules of use; OA articles are governed by the applicable Creative Commons License

68. W. Abd-Elaziem, M. Khedr, A. E. Abd-Elaziem, et al., "Particle-Reinforced Polymer Matrix Composites (PMC) Fabricated by 3D Printing," *Journal of Inorganic and Organometallic Polymers and Materials* 33, no. 12 (2023): 3732–3749.

69. A. Jaisingh Sheoran and H. Kumar, "Fused Deposition Modeling Process Parameters Optimization and Effects on Mechanical Properties and Part Quality: Review and Reflection on Current Research," *Materials Today: Proceedings* 21 (2020): 1659–1672, https://doi.org/10.1016/j.matpr.2019.11.296.

70. G. Ma, Z. Li, L. Wang, F. Wang, and J. Sanjayan, "Mechanical Anisotropy of Aligned fiber-Reinforced Composites for Extrusion-Based 3D Printing," *Construction and Building Materials* 202 (2019): 770–783.

71. S. K. Dhinesh, P. S. Arun, K. K. Senthil, and A. Megalingam, "Study on Flexural and Tensile Behavior of PLA, ABS and PLA–ABS Materials," *Materials Today: Proceedings* 45 (2021): 1175–1180.

72. M. Hussain, S. M. Khan, M. Shafiq, and N. Abbas, "A Review on PLA-Based Biodegradable Materials for Biomedical Applications," *Giant* 18 (2024): 100261.

73. D. Lee and G. Y. Wu, "Parameters Affecting the Mechanical Properties of Three-Dimensional (3D)–printed Carbon fiber–Reinforced Polylactide Composites," *Polymers* 12, no. 11 (2020): 2456.

74. H. Ma, C. Feng, J. Chang, and C. Wu, "3D-Printed Bioceramic Scaffolds: From Bone Tissue Engineering to Tumor Therapy," *Acta Biomaterialia* 79 (2018): 37–59.

75. B. G. Pavan Kalyan and L. Kumar, "3D Printing: Applications in Tissue Engineering, Medical Devices, and Drug Delivery," *AAPS PharmSciTech* 23, no. 4 (2022): 92.

76. A. K. Trivedi, M. K. Gupta, and H. Singh, "PLA Based Biocomposites for Sustainable Products: A Review," *Advanced Industrial and Engineering Polymer Research* 6, no. 4 (2023): 382–395.

77. A. Farazin, C. Zhang, A. Gheisizadeh, and A. Shahbazi, "3D Bioprinting for Use as Bone Replacement Tissues: A Review of Biomedical Applications," *Biomedical Engineering Advances* 5 (2023): 100075.

78. K. M. Percival, V. Paul, and G. A. Husseini, "Recent Advancements in Bone Tissue Engineering: Integrating Smart Scaffold Technologies and Bio-Responsive Systems for Enhanced Regeneration," *International Journal of Molecular Sciences* 25, no. 11 (2024): 6012.

79. A. Tsouknidas, M. Pantazopoulos, and I. Katsoulis, "Impact Absorption Capacity of 3D-Printed Components Fabricated by Fused Deposition Modelling," *Materials & Design* 102 (2016): 41–44, https://doi.org/10.1016/j.matdes.2016.03.154.

80. X. Wang, C. Wang, C. Chu, F. Xue, J. Li, and J. Bai, "Structure–Function Integrated Biodegradable Magnesium/Polymer Composites: Design, Manufacturing, Properties, and Biomedical Applications," *Bioactive Materials* 39 (2024): 74–105.

81. W. Liang, C. Zhou, J. Bai, et al., "Current Developments and Future Perspectives of Nanotechnology in Orthopedic Implants: An Updated Review," *Frontiers in Bioengineering and Biotechnology* 12 (2024): 1342340.

82. C. J. Lodge, H. E. Matar, R. Berber, P. J. Radford, and B. V. Bloch, "Ceramic Coatings Confer no Survivorship Advantage in Total Knee Arthroplasty: A Single-Center Series of 1641 Knees," *Arthroplasty Today* 19 (2023): 101086.

83. E. Marin and A. Lanzutti, "Biomedical Applications of Titanium Alloys: A Comprehensive Review," *Materials* 17, no. 1 (2023): 114.

84. M. S. B. Reddy, D. Ponnamma, R. Choudhary, and K. K. Sadasivuni, "A Comparative Review of Natural and Synthetic Biopolymer Composite Scaffolds," *Polymers* 13, no. 7 (2021): 1105.

85. R. García-Sobrino, M. Muñoz, E. Rodríguez-Jara, J. Rams, B. Torres, and S. C. Cifuentes, "Bioabsorbable Composites Based on Polymeric Matrices (PLA and PCL) Reinforced With Magnesium for Use in Bone Regeneration Therapy: Physicochemical Properties and Biological Evaluation," *Polymers* 15, no. 24 (2023): 4667.

86. V. Hubertus, A. Wagner, C. Albrecht, et al., "Carbon fiber–Reinforced PEEK Implants in Oncologic Spine Surgery: A Multicenter Experience on Implications for Postoperative Patient Management," *Journal of Neurosurgery. Spine* 42, no. 5 (2025): 605–614.

87. T. Zhang, W. Wang, J. Liu, L. Wang, Y. Tang, and K. Wang, "A Review on Magnesium Alloys for Biomedical Applications," *Frontiers in Bioengineering and Biotechnology* 10 (2022): 953344.

88. L. Li, M. Zhang, Y. Li, J. Zhao, L. Qin, and Y. Lai, "Corrosion and Biocompatibility Improvement of Magnesium-Based Alloys as Bone Implant Materials: A Review," *Regenerative Biomaterials* 4, no. 2 (2017): 129–137.

89. Y. Lu, S. Deshmukh, I. Jones, and Y. L. Chiu, "Biodegradable Magnesium Alloys for Orthopaedic Applications," *Biomaterials Translational* 2, no. 3 (2021): 214–235.

90. B. Cong and H. Zhang, "Innovative 3D Printing Technologies and Advanced Materials Revolutionizing Orthopedic Surgery: Current Applications and Future Directions," *Frontiers in Bioengineering and Biotechnology* 13 (2025): 1542179.

91. M. Moradi, S. Meiabadi, and A. Kaplan, "3D-Printed Parts With Honeycomb Internal Patterns Produced by Fused Deposition Modelling: Experimental Characterization and Production Optimization," *Metals and Materials International* 25 (2019): 1312–1325, https://doi.org/10.1007/s12540-019-00272-9.

Supporting Information

Additional supporting information can be found online in the Supporting Information section. **Figure S1:** DSC (left) and TGA (right) thermograms of PLA/SS composites with different SS contents (3–15 wt%). **Figure S2:** Rheological properties (density, MFI, and MVR) of PLA/316 L SS composite filaments with various SS content presented in Figure. **Figure S3:** EDX mapping and point based spectrum analysis. **Figure S4:** Summary of tensile mechanical properties of PLA/SS composites under 0°, 45°, and 90° orientations. Properties include yield strength, ultimate strength, modulus, and strain-to-failure, extracted from the stress–strain curves presented in (Figure 6). **Figure S5:** Summary of compression mechanical properties of PLA/SS composites under 0°, 45°, and 90° orientations. Properties include yield strength, ultimate strength, modulus, and strain-to-failure, extracted from the stress–strain curves presented in (Figure 7). **Table S1:** Taguchi L18 experimental design, mechanical responses, and S/N ratios. **Table S2:** ANOVA summary table for tensile strength. **Table S3:** ANOVA summary table for compressive strength. **Table S4:** ANOVA summary table for impact toughness. **Table S5:** GRA analysis results. **Table S6:** Optimum GRG values for control factor levels. **Table S7:** ANOVA summary table for GRG. **Table S8:** Predicted vs. Experimental Mechanical Properties and Model Accuracy.

15480569, 0, Downloaded from https://4spepublications.onlinelibrary.wiley.com/doi/10.1002/pc.70888 by Gazi University, Wiley Online Library on [04/02/2026]. See the Terms and Conditions (https://onlinelibrary.wiley.com/terms-and-conditions) on Wiley Online Library for rules of use; OA articles are governed by the applicable Creative Commons License